

THE ENVIRONMENTS OF THE MOST ENERGETIC GAMMA-RAY BURSTS

B. P. GOMPERTZ,^{1,2} A. S. FRUCHTER,¹ AND A. PE'ER³

¹*Space Telescope Science Institute, Baltimore, MD 21218, USA*

²*Department of Physics, University of Warwick, Coventry, CV4 7AL, UK*

³*Physics Department, University College Cork, Cork, Ireland*

ABSTRACT

We analyze the properties of a sample of long gamma-ray bursts (LGRBs) detected by the Fermi satellite that have a spectroscopic redshift and good follow-up coverage at both X-ray and optical/nIR wavelengths. The evolution of LGRB afterglows depends on the density profile of the external medium, enabling us to separate wind or ISM-like environments based on the observations. We do this by identifying the environment that provides the best agreement between estimates of p , the index of the underlying power-law distribution of electron energies, as determined by the behavior of the afterglow in different spectral/temporal regimes. At 11 rest-frame hours after trigger, we find a roughly even split between ISM-like and wind-like environments. We further find a 2σ separation in the prompt emission energy distributions of wind-like and ISM-like bursts. We investigate the underlying physical parameters of the shock, and calculate the (degenerate) product of density and magnetic field energy (ϵ_B). We show that ϵ_B must be $\ll 10^{-2}$ to avoid implied densities comparable to the intergalactic medium. Finally, we find that the most precisely constrained observations disagree on p by more than would be expected based on observational errors alone. This suggests additional sources of error that are not incorporated in the standard afterglow theory. For the first time, we provide a measurement of this intrinsic error which can be represented as an error in the estimate of p of magnitude 0.25 ± 0.04 . When this error is included in the fits, the number of LGRBs with an identified environment drops substantially, but the equal division between the two types remains.

1. INTRODUCTION

Long gamma-ray bursts (LGRBs) are well established as core-collapse events following the deaths of massive stars, due to their close proximity to very young star forming regions (Fruchter et al. 2006; Levesque et al. 2010) and consistent association with type Ic supernovae (e.g. Hjorth et al. 2003; Cano 2013). Their emission is best modelled as a collimated jet of relativistic material that is launched from the central star by the initial collapse (cf. Woosley 1993). The γ -rays are widely believed to be produced by dissipation of either kinetic (e.g. Paczynski 1986; Rees & Meszaros 1992) or magnetic (e.g. Usov 1994; Drenkhahn & Spruit 2002; Zhang & Yan 2011) energy in the expanding jet.

The expanding jet collides with material in the circumstellar environment, causing it to decelerate. As it moves at relativistic speeds, a shock wave is formed (Blandford & McKee 1976). The shock is believed to accelerate particles to high energies as well as generate a strong magnetic field. The heated particles in turn emit a broad-band radiation (mainly via synchrotron and possibly Compton) known as the ‘afterglow’, with emission ranging from X-rays to radio frequencies.

Broad-band fitting of LGRB afterglows suggests that they can occur in at least two different types of environment (Chevalier & Li 1999): interstellar medium (ISM)-like environments, in which the density of the circumstellar material does not change with distance from the central object, or wind-like environments, in which the density falls as r^{-2} . The latter case should occur when the progenitor star possessed a strong stellar wind in its final stages of life before collapse (Chevalier & Li 2000). The former may be the result of a progenitor star with a very weak stellar wind, so that the expanding fireball quickly crosses from the wind-like environment into a homogeneous density region at larger radii (see e.g. Pe’er & Wijers 2006; van Marle et al. 2006).

LGRB afterglows are generally well explained by synchrotron theory (Rees & Meszaros 1992; Wijers et al. 1997; Sari et al. 1998; Wijers & Galama 1999; Granot et al. 2002; Gao et al. 2013). It is assumed that electrons at the shock front are accelerated to a power-law distribution of the form $N(\gamma_e)d\gamma_e \propto \gamma_e^{-p}d\gamma_e$, above a minimum Lorentz factor γ_m . γ_e is the electron’s Lorentz factor. Here the power-law index is $p > 2$. The shape of the distribution means that the minimum Lorentz factor is also the most common, and represents the peak frequency (ν_m) of the synchrotron spectrum. At sufficiently high frequencies, the radiative cooling time equals the dynamical time, which is the time available to cool. As a result, above the cooling break (ν_c), the steady state distribution of the electrons, resulting from both rapid acceleration and cooling, steepens. Finally, at low frequencies the emitted photons are more easily re-absorbed by the emitting material, and this creates a third break in the synchrotron spectrum: the self-absorption frequency ν_a .

The positions of these breaks are functions of the physical properties of the plasma flow, such as the energy, magnetic field, density and available time. While there is some knowledge about, e.g., the available energy, the values of parameters like the magnetic field strength and the density are highly uncertain. Nonetheless, these parameters combine to describe a spectrum comprised of four power-law segments smoothly connected by three spectral breaks: ν_a , ν_m and ν_c . At times of around half a day post-burst, ν_c is typically found close to X-ray frequencies in LGRBs, with ν_m at optical/near infra-red (nIR) frequencies and ν_a down at radio wavelengths.

Because the synchrotron spectrum is sensitive to density, its evolution can be used to diagnose the type of environment into which the GRB afterglow is expanding. The theoretical relation between p , the spectral index β , and the tem-

poral index α is given by the synchrotron closure relations, which vary between environment types and in different regions of the synchrotron spectrum. We use the convention $F \propto t^{-\alpha} \nu^{-\beta}$ when discussing them.

As early as a few years after the detection of the first LGRB optical afterglow (van Paradijs et al. 1997) a split between ISM-like and wind-like environments was observed, with up to 50 per cent of bursts found to be consistent with a homogeneous medium (e.g. Chevalier & Li 2000; Panaitescu & Kumar 2001, 2002). In later studies, (e.g. Starling et al. 2008; Curran et al. 2009) ISM-like environments continued to be found in LGRB afterglows. Schulze et al. (2011) studied the environments of a sample of 26 *Swift* LGRBs (and one SGRB), finding just 6 that showed a wind-like evolution at late times. 18 were classed as ISM-like. Measurements of the spectral and temporal indices for optical (Oates et al. 2012) and X-ray (Oates et al. 2015; Racusin et al. 2016) afterglows of LGRBs all point to a split in environment types between wind and ISM. In the largest previous study to date, Li et al. (2015) investigated the X-ray and optical slopes of a large sample of 87 GRBs (80 with redshift) discovered by the *Swift* satellite up until 2013, finding that 61 per cent of them were consistent with an ISM-like medium, while just 39 per cent appeared wind-like.

Given the apparent prevalence of ISM-like environments, the signature of the afterglow emission site transitioning across a termination shock from a wind-like to an ISM-like medium (e.g. Dai & Lu 2002) should in theory be commonly observed within the LGRB afterglow population. However, despite several claims (Dai & Wu 2003; Jin et al. 2009; Feng & Dai 2011; Veres et al. 2015), such a signature has never been unambiguously identified. LGRBs therefore warrant further investigations into their environment types, their energies, and the underlying physical parameters of their af-

terglows. These properties may provide clues as to why a termination shock transition has not been observed. Obtaining a large sample with known redshift allows for well-defined energetics, which provides a previously unexplored attribute when making comparisons between the identified environment types.

In this paper, we investigate the energetics and environments of a sample of 56 *Fermi*-discovered LGRBs, all of which have an identified redshift and detections in both X-rays and optical/nIR. We include bursts observed by both the Large Area Telescope (LAT; Atwood et al. 2009) and the Gamma-ray Burst Monitor (GBM; Meegan et al. 2009), and those seen by the GBM only. Contrary to previous works, we discriminate between the different environment types based on several independent measures: the observed spectral and temporal indices, and the measured ratio of their optical-to-X-ray fluxes (F_R/F_X) where appropriate. The increased bandpass of GBM compared to *Swift*-BAT also allows us to better constrain the isotropic equivalent γ -ray energy ($E_{\gamma,iso}$) of each burst and compare it across the sample. This enables us for the first time to make statistical comparisons between environment types based on burst energies.

In Section 2 we introduce the data collected for the sample. Section 3 describes how we ascertain the environment type for each burst. Our results are presented in Section 4, and are discussed in Section 5. We outline our conclusions in Section 6. We use a cosmology of $H_0 = 67.8 \text{ km s}^{-1} \text{ Mpc}^{-1}$, $\Omega_M = 0.308$ and $\Omega_\Lambda = 0.692$ (Planck Collaboration et al. 2016) throughout this paper.

2. DATA

We collected all LGRBs that were detected by the *Fermi* satellite, had been observed by both *Swift*-XRT and ground-based optical/nIR telescopes, and had an identified redshift. Our sample is the largest and most comprehensive col-

lection of *Fermi*-discovered GRBs with redshift and multi-wavelength observations, comprising 56 events.

2.1. Prompt Data

To calculate the isotropic γ -ray energy release, $E_{\gamma, \text{iso}}$, we take the GBM fluence measured in the 10 - 1000 keV bandpass from the *Fermi*-GBM catalogue (Gruber et al. 2014; von Kienlin et al. 2014; Narayana Bhat et al. 2016). Comparing energies between bursts of different redshifts requires a cosmological k-correction (Bloom et al. 2001) in order to account for the shift in the observer frame bandpass, and this requires knowledge of the spectral shape of the prompt emission. GRB prompt emission spectra are usu-

ally fitted with the Band function (Band et al. 1993), comprised of a low-energy spectral index a , a peak energy E_p , and a high energy spectral index b . Taking the Band function spectral parameters from the *Fermi*-GBM catalogue (Gruber et al. 2014; von Kienlin et al. 2014; Narayana Bhat et al. 2016), we convert the observer frame 10 - 1000 keV fluence into $E_{\gamma, \text{iso}}$ between 10 - 1000 keV in the *rest* frame for each burst. This is one area in which our work has a significant advantage over studies done with *Swift*-BAT, since the BAT bandpass of 15 - 150 keV often does not capture E_p , making the true prompt emission energy uncertain. Our prompt emission parameters, including k-corrected energies, are displayed in Table 1.

GRB	z	Fluence (erg cm ⁻²)	T ₉₀ (s)	E_p (keV)	a	b	$E_{\gamma, \text{iso}}$ (erg)
LAT							
080916C	4.35 ⁽¹⁾	$(6.03 \pm 0.01) \times 10^{-5}$	63.0 ± 0.81	662 ± 45	1.08 ± 0.01	2.15 ± 0.07	$(7.84 \pm 0.01) \times 10^{53}$
090323	3.44 ⁽²⁾	$(11.8 \pm 0.02) \times 10^{-5}$	135 ± 1.45	633 ± 41	1.28 ± 0.01	2.44 ± 0.17	$(16.7 \pm 0.02) \times 10^{53}$
090328A	0.74 ⁽²⁾	$(4.20 \pm 0.01) \times 10^{-5}$	62.0 ± 1.81	640 ± 46	1.09 ± 0.02	2.37 ± 0.18	$(4.90 \pm 0.01) \times 10^{52}$
090902B	1.24 ⁽²⁾	$(22.2 \pm 0.03) \times 10^{-5}$	19.3 ± 0.29	1055 ± 17	1.01 ± 0.004	11.8 ± 4018	$(8.98 \pm 0.01) \times 10^{53}$
090926A	2.11 ⁽³⁾	$(14.7 \pm 0.03) \times 10^{-5}$	13.8 ± 0.29	340 ± 6	0.86 ± 0.01	2.40 ± 0.04	$(9.50 \pm 0.02) \times 10^{53}$
091003	0.90 ⁽⁴⁾	$(2.33 \pm 0.01) \times 10^{-5}$	20.2 ± 0.36	367 ± 27	1.07 ± 0.02	2.23 ± 0.11	$(4.20 \pm 0.01) \times 10^{52}$
091208B	1.06 ⁽⁵⁾	$(6.19 \pm 0.19) \times 10^{-6}$	12.5 ± 5.02	38 ± 6	0.15 ± 0.39	1.90 ± 0.04	$(1.52 \pm 0.05) \times 10^{52}$
100414A	1.37 ⁽⁶⁾	$(8.85 \pm 0.02) \times 10^{-5}$	26.5 ± 2.07	664 ± 16	0.62 ± 0.01	3.54 ± 0.49	$(21.0 \pm 0.04) \times 10^{52}$
100728A	1.57 ⁽⁷⁾	$(1.28 \pm 0.01) \times 10^{-4}$	165 ± 2.90	290 ± 8	0.64 ± 0.02	2.70 ± 0.15	$(5.34 \pm 0.02) \times 10^{53}$
110731A	2.83 ⁽⁸⁾	$(2.29 \pm 0.01) \times 10^{-8}$	7.49 ± 0.57	319 ± 20	0.87 ± 0.03	2.44 ± 0.16	$(2.19 \pm 0.01) \times 10^{53}$
120711A	1.41 ⁽⁹⁾	$(19.4 \pm 0.02) \times 10^{-5}$	44.0 ± 0.72	1319 ± 46	0.98 ± 0.01	2.80 ± 0.09	$(5.17 \pm 0.01) \times 10^{53}$
130427A	0.34 ⁽¹⁰⁾	$(24.6 \pm 0.01) \times 10^{-4}$	138 ± 3.24	830 ± 5^a	0.79 ± 0.003^a	3.06 ± 0.02^a	$(60.8 \pm 0.03) \times 10^{52}$
130518A	2.49 ⁽¹¹⁾	$(9.46 \pm 0.02) \times 10^{-5}$	48.6 ± 0.92	398 ± 16	0.91 ± 0.02	2.25 ± 0.07	$(7.21 \pm 0.01) \times 10^{53}$
130907A	1.24 ⁽¹²⁾	$(7.9 \pm 0.5) \times 10^{-4}^\dagger$	-	394 ± 11^b	0.65 ± 0.03^b	2.22 ± 0.05^b	$(2.32 \pm 0.15) \times 10^{54}$
131108A	2.4 ⁽¹³⁾	$(3.57 \pm 0.01) \times 10^{-5}$	18.2 ± 0.57	367 ± 18	0.91 ± 0.02	2.46 ± 0.15	$(2.73 \pm 0.01) \times 10^{53}$
131231A	0.64 ⁽¹⁴⁾	$(15.2 \pm 0.01) \times 10^{-5}$	31.2 ± 0.57	178 ± 4	1.21 ± 0.01	2.30 ± 0.03	$(16.1 \pm 0.01) \times 10^{52}$
141028A	2.33 ⁽¹⁵⁾	$(3.48 \pm 0.01) \times 10^{-5}$	31.5 ± 2.43	294 ± 16	0.84 ± 0.03	1.97 ± 0.04	$(2.51 \pm 0.01) \times 10^{53}$
150314A	1.76 ⁽¹⁶⁾	$(8.16 \pm 0.01) \times 10^{-5}$	10.7 ± 0.14	347 ± 7	0.68 ± 0.01	2.60 ± 0.08	$(3.73 \pm 0.01) \times 10^{53}$

GRB	z	Fluence (erg cm ⁻²)	T ₉₀ (s)	E _p (keV)	a	b	E _{γ,iso} (erg)
150403A	2.06 ⁽¹⁷⁾	$(5.47 \pm 0.01) \times 10^{-5}$	22.3 ± 0.81	429 ± 17	0.87 ± 0.02	2.11 ± 0.04	$(30.9 \pm 0.03) \times 10^{52}$
150514A	0.81 ⁽¹⁸⁾	$(4.74 \pm 0.05) \times 10^{-6}$	10.8 ± 1.07	65 ± 6	1.21 ± 0.10	2.43 ± 0.13	$(8.67 \pm 0.09) \times 10^{51}$
160509A	1.17 ⁽¹⁹⁾	$(17.9 \pm 0.02) \times 10^{-5}$	370 ± 0.81	355 ± 10	1.02 ± 0.01	2.23 ± 0.04	$(50.7 \pm 0.04) \times 10^{52}$
160623A	0.37 ⁽²⁰⁾	$(3.96 \pm 0.07) \times 10^{-6}$	108 ± 8.69	999 ± 4630	1.49 ± 0.17	1.61 ± 0.15	$(1.25 \pm 0.02) \times 10^{51}$
160625B	1.41 ⁽²¹⁾	$(5.69 \pm 0.01) \times 10^{-4}$	455 ± 11.0	649 ± 9	0.95 ± 0.003	2.37 ± 0.03	$(17.7 \pm 0.03) \times 10^{53}$
GBM							
080916A	0.69 ⁽²²⁾	$(7.81 \pm 0.08) \times 10^{-6}$	46.3 ± 7.17	107 ± 19	0.82 ± 0.13	1.78 ± 0.05	$(8.38 \pm 0.09) \times 10^{51}$
081007	0.53 ⁽²³⁾	$(1.20 \pm 0.10) \times 10^{-6c}$	$\sim 12^c$	40 ± 10^c	1.4 ± 0.4^c	8^c+	$(1.06 \pm 0.09) \times 10^{51}$
081121	2.51 ⁽²⁴⁾	$(1.53 \pm 0.02) \times 10^{-5}$	42.0 ± 8.51	161 ± 17	0.43 ± 0.13	2.09 ± 0.09	$(1.26 \pm 0.02) \times 10^{53}$
090423	8.23 ⁽²⁵⁾	$(8.16 \pm 0.72) \times 10^{-7}$	7.17 ± 2.42	66 ± 16	0.59 ± 0.50	2.67 ± 0.74	$(4.45 \pm 0.39) \times 10^{52}$
090424	0.54 ⁽²⁶⁾	$(46.3 \pm 0.04) \times 10^{-6}$	14.1 ± 0.26	154 ± 4	1.04 ± 0.02	2.76 ± 0.12	$(36.2 \pm 0.03) \times 10^{51}$
090618	0.54 ⁽²⁷⁾	$(26.8 \pm 0.04) \times 10^{-5}$	112 ± 1.09	147 ± 4	1.13 ± 0.01	2.22 ± 0.02	$(20.0 \pm 0.03) \times 10^{52}$
091020	1.71 ⁽²⁸⁾	$(1.07 \pm 0.01) \times 10^{-5}$	37.5 ± 0.91	1193 ± 239	0.99 ± 0.05	2.71 ± 0.61	$(5.78 \pm 0.10) \times 10^{52}$
091127	0.49 ⁽²⁹⁾	$(20.7 \pm 3.70) \times 10^{-6}$	8.70 ± 0.57	35 ± 2	1.26 ± 0.07	2.22 ± 0.02	$(13.8 \pm 0.02) \times 10^{51}$
100906A	1.73 ⁽³⁰⁾	$(2.33 \pm 0.01) \times 10^{-5}$	111 ± 2.83	70 ± 10	0.90 ± 0.13	1.86 ± 0.03	$(13.3 \pm 0.03) \times 10^{52}$
101219B	0.55 ⁽³¹⁾	$(3.99 \pm 0.05) \times 10^{-6}$	51.0 ± 1.78	56 ± 7	-1.37 ± 0.72	2.26 ± 0.14	$(2.85 \pm 0.03) \times 10^{51}$
110213A	1.46 ⁽³²⁾	$(9.37 \pm 0.05) \times 10^{-6}$	34.3 ± 1.64	75 ± 13	1.42 ± 0.09	2.13 ± 0.09	$(5.13 \pm 0.03) \times 10^{52}$
111228A	0.71 ⁽³³⁾	$(1.81 \pm 0.01) \times 10^{-5}$	99.8 ± 2.11	27 ± 1	1.58 ± 0.08	2.44 ± 0.06	$(3.00 \pm 0.01) \times 10^{52}$
120119A	1.73 ⁽³⁴⁾	$(3.87 \pm 0.01) \times 10^{-5}$	55.3 ± 6.23	183 ± 8	0.96 ± 0.03	2.37 ± 0.09	$(2.36 \pm 0.01) \times 10^{53}$
120729A	0.80 ⁽³⁵⁾	$(5.08 \pm 0.05) \times 10^{-6}$	25.5 ± 2.61	26 ± 168	0.06 ± 30.5	1.62 ± 0.04	$(6.83 \pm 0.07) \times 10^{51}$
120811C	2.67 ⁽³⁶⁾	$(3.45 \pm 0.21) \times 10^{-6}$	14.3 ± 6.56	56 ± 5	0.71 ± 0.27	2.85 ± 0.32	$(5.40 \pm 0.33) \times 10^{52}$
121211A	1.02 ⁽³⁷⁾	$(6.41 \pm 0.40) \times 10^{-7}$	5.62 ± 1.72	100 ± 16	0.27 ± 0.37	4.80 ± 15.9	$(1.79 \pm 0.11) \times 10^{51}$
130420A	1.30 ⁽³⁸⁾	$(1.16 \pm 0.02) \times 10^{-5}$	105 ± 8.81	57 ± 3	1.13 ± 0.12	10.6 ± 1405	$(5.99 \pm 0.13) \times 10^{52}$
140213A	1.21 ⁽³⁹⁾	$(2.12 \pm 0.01) \times 10^{-5}$	18.6 ± 0.72	87 ± 4	1.13 ± 0.03	2.26 ± 0.05	$(7.82 \pm 0.02) \times 10^{52}$
140423A	3.26 ⁽⁴⁰⁾	$(1.81 \pm 0.01) \times 10^{-5}$	95.2 ± 11.6	121 ± 15	0.60 ± 0.12	1.83 ± 0.05	$(2.09 \pm 0.01) \times 10^{53}$
140506A	0.89 ⁽⁴¹⁾	$(6.59 \pm 0.12) \times 10^{-6}$	64.1 ± 2.01	198 ± 33	1.18 ± 0.11	9.80 ± 2845	$(1.43 \pm 0.03) \times 10^{52}$
140512A	0.73 ⁽⁴²⁾	$(2.93 \pm 0.01) \times 10^{-5}$	148 ± 2.36	683 ± 70	1.22 ± 0.02	3.24 ± 1.64	$(3.46 \pm 0.01) \times 10^{52}$
140606B	0.38 ⁽⁴³⁾	$(7.59 \pm 0.04) \times 10^{-6}$	22.8 ± 2.06	555 ± 165	1.24 ± 0.05	2.20 ± 0.52	$(2.71 \pm 0.02) \times 10^{51}$
140620A	2.04 ⁽⁴⁴⁾	$(6.15 \pm 0.06) \times 10^{-6}$	45.8 ± 12.1	76 ± 11	0.93 ± 0.16	2.15 ± 0.09	$(5.24 \pm 0.05) \times 10^{52}$
140703A	3.14 ⁽⁴⁵⁾	$(7.57 \pm 0.05) \times 10^{-6}$	84.0 ± 3.00	208 ± 36	1.27 ± 0.06	2.61 ± 0.79	$(1.32 \pm 0.01) \times 10^{53}$
140801A	1.32 ⁽⁴⁶⁾	$(12.4 \pm 0.04) \times 10^{-6}$	7.17 ± 0.57	119 ± 3	0.38 ± 0.04	3.93 ± 0.66	$(5.32 \pm 0.02) \times 10^{52}$
140907A	1.21 ⁽⁴⁷⁾	$(6.45 \pm 0.06) \times 10^{-6}$	35.8 ± 5.47	141 ± 10	1.03 ± 0.06	14.7 ± 10^6	$(2.58 \pm 0.03) \times 10^{52}$
141004A	0.57 ⁽⁴⁸⁾	$(1.18 \pm 0.03) \times 10^{-6}$	2.56 ± 0.61	28 ± 11	-0.10 ± 1.68	1.91 ± 0.08	$(9.27 \pm 0.26) \times 10^{50}$

GRB	z	Fluence (erg cm ⁻²)	T ₉₀ (s)	E _p (keV)	a	b	E _{γ,iso} (erg)
150301B	1.52 ⁽⁴⁹⁾	$(3.09 \pm 0.03) \times 10^{-6}$	13.3 ± 1.56	183 ± 36	1.05 ± 0.10	2.22 ± 0.28	$(1.52 \pm 0.01) \times 10^{52}$
150821A	0.76 ⁽⁵⁰⁾	$(5.21 \pm 0.03) \times 10^{-5}$	103 ± 5.75	281 ± 18	1.24 ± 0.02	2.13 ± 0.07	$(7.21 \pm 0.04) \times 10^{52}$
151027A	0.81 ⁽⁵¹⁾	$(1.41 \pm 0.01) \times 10^{-5}$	123 ± 1.15	203 ± 34	1.25 ± 0.05	1.96 ± 0.08	$(2.21 \pm 0.01) \times 10^{52}$
160804A	0.74 ⁽⁵²⁾	$(1.62 \pm 0.02) \times 10^{-5}$	132 ± 21.7	71 ± 4	1.03 ± 0.09	2.82 ± 0.90	$(2.47 \pm 0.04) \times 10^{52}$
161017A	2.01 ⁽⁵³⁾	$(5.42 \pm 0.13) \times 10^{-6}$	32.3 ± 8.08	239 ± 41	1.03 ± 0.10	2.37 ± 0.78	$(4.05 \pm 0.09) \times 10^{52}$
170113A	1.97 ⁽⁵⁴⁾	$(2.04 \pm 0.08) \times 10^{-6}$	49.2 ± 4.14	113 ± 59	1.70 ± 0.22	10 ¹¹	$(2.59 \pm 0.10) \times 10^{52}$

Table 1. The prompt emission properties of the sample. Fluence is 10 – 1000 keV in the observer frame unless marked. $E_{\gamma,iso}$ values have been k-corrected (Bloom et al. 2001) to 10 – 1000 keV in the rest frame. Fluence, T₉₀, E_p, α and β come from the *Fermi*-GBM catalogue (Gruber et al. 2014; von Kienlin et al. 2014; Narayana Bhat et al. 2016) unless otherwise marked.

^avon Kienlin (2013); ^bGolenetskii et al. (2013); ^cBissaldi et al. (2008); [†]Seen by LAT but not by GBM, so the tabulated fluence is from *Konus-Wind* in the 20 keV – 10 MeV range; ⁺The best fit is an exponential cutoff, which we model with an index of 8.

Redshift references: (1) - Greiner et al. (2009); (2) - McBreen et al. (2010); (3) - D’Elia et al. (2010); (4) - Cucchiara et al. (2009b); (5) - Wiersema et al. (2009b); (6) - Cucchiara & Fox (2010); (7) - Krühler et al. (2015); (8) - Tanvir et al. (2011); (9) - Tanvir et al. (2012); (10) - Levan et al. (2014); (11) - Sanchez-Ramirez et al. (2013); (12) - de Ugarte Postigo et al. (2013c); (13) - de Ugarte Postigo et al. (2013b); (14) - Xu et al. (2014b); (15) - Xu et al. (2014a); (16) - de Ugarte Postigo et al. (2015c); (17) - Pugliese et al. (2015); (18) - de Ugarte Postigo et al. (2015b); (19) - Tanvir et al. (2016); (20) - Malesani et al. (2016); (21) - Xu et al. (2016b); (22) - Fynbo et al. (2008); (23) - Berger et al. (2008); (24) - Berger & Rauch (2008); (25) - Tanvir et al. (2009); (26) - Chornock et al. (2009); (27) - Cenko et al. (2009); (28) - Xu et al. (2009); (29) - Cucchiara et al. (2009a); (30) - Tanvir et al. (2010); (31) - de Ugarte Postigo et al. (2011); (32) - Milne & Cenko (2011); (33) - Dittmann et al. (2011); (34) - Cucchiara & Prochaska (2012); (35) - Tanvir & Ball (2012); (36) - Thoene et al. (2012); (37) - Perley et al. (2012); (38) - de Ugarte Postigo et al. (2013a); (39) - Schulze et al. (2014); (40) - Tanvir et al. (2014); (41) - Fynbo et al. (2014a); (42) - de Ugarte Postigo et al. (2014b); (43) - Singer et al. (2015); (44) - Kasliwal et al. (2014); (45) - Castro-Tirado et al. (2014b); (46) - de Ugarte Postigo et al. (2014a); (47) - Castro-Tirado et al. (2014a); (48) - de Ugarte Postigo et al. (2014c); (49) - de Ugarte Postigo et al. (2015a); (50) - D’Elia et al. (2015); (51) - Perley et al. (2015); (52) - Xu et al. (2016a); (53) - de Ugarte Postigo et al. (2016); (54) - Xu et al. (2017)

2.2. X-ray Data

The X-ray data (Table 2) come almost exclusively from the UK *Swift* Science Data Centre (UKSSDC; Evans et al. 2007, 2009)¹. For each GRB, the data point closest to 11 h in the rest frame is identified. The *Swift*-XRT GRB catalog automatically fits the X-ray light curves with a broken power law model, and we take

the temporal and spectral² indices for the power law segment local to the selected data point. Absorption is accounted for by taking the ratio of the unabsorbed counts-to-flux over the observed counts-to-flux from the spectrum of the local power law, and applying it as a multiplication factor to the flux. We then convert to flux

² The UKSSDC actually gives the photon index, Γ_x , where the spectral index $\beta_x = \Gamma_x - 1$

¹ www.swift.ac.uk

density via (cf. Gehrels et al. 2008):

$$F_{\nu,x} = 4.13 \times 10^{11} \frac{F_x(2 - \Gamma_x)E_0^{1-\Gamma_x}}{(E_2^{2-\Gamma_x} - E_1^{2-\Gamma_x})} \mu\text{Jy}, \quad (1)$$

where E_1 and E_2 are the lower and upper bounds of the bandpass in keV, E_0 is the target energy for the flux density in keV, F_x is the measured flux in $\text{erg cm}^{-2} \text{s}^{-1}$, and Γ_x is the estimated unabsorbed X-ray photon index. A k-correction (cf. Bloom et al. 2001) is applied to the flux density to account for the disparate redshifts of the rest frame bandpass between bursts, which keeps the results comparable between GRBs at different cosmological distances. Note that these may not be the same values for k as in the E_{iso} calculations in Table 1 due to the spectral break in the Band function. The flux densities are then extrapolated to 11 hours rest-frame using the identified temporal index α_x , and to 5 keV in the rest frame ($5 \times (1+z)$ keV)

using β_x . We use 5 keV because at this energy the error in the flux density, caused by the uncertainty in the estimate of intrinsic absorption, is relatively small.

Due to the mis-identification of flares, for some bursts the UKSSDC automatic fitting routine gives obviously erroneous results. For these cases, we manually fit the X-ray light curves to obtain the local temporal index, then run the UKSSDC time slice spectrum routine for the identified power law segment to ascertain the local spectral index and counts-to-flux ratio. The affected bursts are GRB 100728A and GRB 120119A. For four bursts in the sample, we have additional X-ray observations from *Chandra* (Fruchter et al. in prep). In these cases, we again fit the light curves manually to find the temporal indices, and use the UKSSDC time slice spectrum tool to find the spectral index for the local power law segment. The four bursts are GRBs 110731A, 120711A, 130427A and 150314A.

GRB	$t_{x,\text{rest}}$ (h)	$F_{x[0.3-10\text{keV}]}$ ($\text{erg cm}^{-2} \text{s}^{-1}$)	α_x	Γ_x	Absorption Correction	k	$F_{\nu,x[5\text{keV}]}$ (μJy)
LAT							
080916C	9.66	$(1.41 \pm 0.39) \times 10^{-13}$	$1.31^{+0.09}_{-0.08}$	$1.80^{+0.30}_{-0.24}$	1.44	0.13	$(2.43 \pm 0.66) \times 10^{-3}$
090323	11.20	$(2.88 \pm 0.71) \times 10^{-13}$	$1.61^{+0.09}_{-0.09}$	$1.88^{+0.12}_{-0.13}$	1.04	0.25	$(5.64 \pm 1.38) \times 10^{-3}$
090328A	10.11	$(2.80 \pm 0.58) \times 10^{-12}$	$1.69^{+0.08}_{-0.07}$	$1.55^{+0.19}_{-0.18}$	1.19	0.61	$(6.02 \pm 1.24) \times 10^{-2}$
090902B	10.90	$(1.58 \pm 0.30) \times 10^{-12}$	$1.40^{+0.04}_{-0.03}$	$1.74^{+0.09}_{-0.08}$	1.27	0.27	$(3.45 \pm 0.64) \times 10^{-2}$
090926A	12.91	$(7.90 \pm 2.08) \times 10^{-13}$	$1.41^{+0.03}_{-0.03}$	$1.98^{+0.09}_{-0.09}$	1.13	0.37	$(2.54 \pm 0.67) \times 10^{-2}$
091003	9.36	$(2.28 \pm 0.53) \times 10^{-12}$	$1.36^{+0.04}_{-0.04}$	$1.69^{+0.10}_{-0.10}$	1.14	0.43	$(4.35 \pm 1.00) \times 10^{-2}$
091208B	10.63	$(6.77 \pm 1.08) \times 10^{-13}$	$1.09^{+0.03}_{-0.04}$	$1.89^{+0.09}_{-0.09}$	1.37	0.44	$(2.02 \pm 0.32) \times 10^{-2}$
100414A	20.56	$(9.28 \pm 2, 32) \times 10^{-13}$	$2.53^{+0.12}_{-0.27}$	$1.50^{+0.24}_{-0.24}$	1.11	0.27	$(7.34 \pm 1.84) \times 10^{-2}$
100728A	9.40	$(1.09 \pm 0.26) \times 10^{-12}$	$1.56^{+0.03\dagger}_{-0.03}$	$1.79^{+0.05}_{-0.05}$	1.41	0.30	$(2.33 \pm 0.56) \times 10^{-2}$
110731A	10.47	$(3.10 \pm 0.86) \times 10^{-13}$	$1.21^{+0.01\dagger}_{-0.01}$	$1.83^{+0.07}_{-0.06}$	1.35	0.20	$(7.01 \pm 1.93) \times 10^{-3}$
120711A	11.62	$(6.25 \pm 1.41) \times 10^{-12}$	$1.64^{+0.01\dagger}_{-0.01}$	$1.77^{+0.04}_{-0.04}$	1.34	0.34	$(1.80 \pm 0.41) \times 10^{-1}$
130427A	11.00	$(5.34 \pm 1.21) \times 10^{-11}$	$1.32^{+0.01\dagger}_{-0.01}$	$1.69^{+0.02}_{-0.02}$	1.12	0.68	$(1.55 \pm 0.35) \times 10^0$
130518A	5.94	$(7.96 \pm 1.52) \times 10^{-13}$	$1.26^{+0.13}_{-0.10}$	$2.06^{+0.22}_{-0.15}$	1.50	0.31	$(1.41 \pm 0.27) \times 10^{-2}$
130907A	10.93	$(7.16 \pm 1.36) \times 10^{-12}$	$1.69^{+0.01}_{-0.01}$	$1.87^{+0.02}_{-0.02}$	1.27	0.46	$(1.94 \pm 0.37) \times 10^{-1}$

GRB	$t_{x,\text{rest}}$ (h)	$F_x [0.3-10\text{keV}]$ ($\text{erg cm}^{-2} \text{ s}^{-1}$)	α_x	Γ_x	Absorption Correction	k	$F_{\nu,x} [5\text{keV}]$ (μJy)
131108A	12.04	$(7.88 \pm 1.82) \times 10^{-14}$	$1.33^{+0.04}_{-0.04}$	$1.97^{+0.12}_{-0.11}$	1.22	0.32	$(2.41 \pm 0.56) \times 10^{-3}$
131231A	24.30	$(4.50 \pm 0.97) \times 10^{-12}$	$1.45^{+0.04}_{-0.03}$	$1.79^{+0.08}_{-0.08}$	1.17	0.55	$(3.90 \pm 0.84) \times 10^{-1}$
141028A	10.04	$(3.44 \pm 0.88) \times 10^{-13}$	$0.70^{+0.36}_{-0.49}$	$2.40^{+0.55}_{-0.43}$	1.67	0.49	$(2.03 \pm 0.52) \times 10^{-2}$
150314A	10.69	$(9.96 \pm 1.92) \times 10^{-13}$	$1.50^{+0.06}_{-0.06} \dagger$	$1.84^{+0.05}_{-0.05}$	1.27	0.31	$(2.43 \pm 0.47) \times 10^{-2}$
150403A	11.04	$(4.33 \pm 0.98) \times 10^{-12}$	$1.51^{+0.02}_{-0.02}$	$1.80^{+0.04}_{-0.04}$	1.17	0.23	$(9.23 \pm 2.08) \times 10^{-2}$
150514A	7.23	$(1.27 \pm 0.33) \times 10^{-12}$	$1.26^{+0.18}_{-0.14}$	$1.80^{+0.33}_{-0.12}$	1.04	0.49	$(1.75 \pm 0.46) \times 10^{-2}$
160509A	11.20	$(9.11 \pm 2.06) \times 10^{-12}$	$1.26^{+0.04}_{-0.04}$	$2.02^{+0.06}_{-0.06}$	1.71	0.48	$(3.80 \pm 0.86) \times 10^{-1}$
160623A	10.49	$(3.44 \pm 0.61) \times 10^{-11}$	$1.67^{+0.06}_{-0.06}$	$1.85^{+0.09}_{-0.09}$	1.90	0.70	$(1.51 \pm 0.27) \times 10^0$
160625B	11.16	$(9.37 \pm 2.11) \times 10^{-12}$	$1.21^{+0.02}_{-0.02}$	$1.85^{+0.06}_{-0.06}$	1.22	0.37	$(2.41 \pm 0.54) \times 10^{-1}$
GBM							
080916A	11.44	$(5.68 \pm 1.23) \times 10^{-13}$	$1.24^{+0.05}_{-0.05}$	$2.13^{+0.10}_{-0.10}$	1.61	0.63	$(2.22 \pm 0.48) \times 10^{-2}$
081007	10.86	$(1.05 \pm 0.23) \times 10^{-12}$	$1.18^{+0.07}_{-0.04}$	$2.02^{+0.12}_{-0.15}$	1.55	0.65	$(3.76 \pm 0.82) \times 10^{-2}$
081121	10.84	$(9.52 \pm 2.49) \times 10^{-13}$	$1.42^{+0.01}_{-0.01}$	$1.80^{+0.05}_{-0.04}$	1.11	0.24	$(1.78 \pm 0.47) \times 10^{-2}$
090423	9.44	$(1.91 \pm 0.59) \times 10^{-14}$	$1.41^{+0.05}_{-0.04}$	$1.86^{+0.12}_{-0.12}$	1.18	0.08	$(2.67 \pm 0.82) \times 10^{-4}$
090424	6.57	$(7.19 \pm 1.42) \times 10^{-12}$	$1.09^{+0.02}_{-0.02}$	$1.84^{+0.05}_{-0.05}$	1.31	0.60	$(1.28 \pm 0.25) \times 10^{-1}$
090618	10.76	$(7.02 \pm 1.36) \times 10^{-12}$	$1.74^{+0.04}_{-0.04} (1)$	$1.80^{+0.03}_{-0.02}$	1.23	0.60	$(2.03 \pm 0.39) \times 10^{-1}$
091020	11.70	$(2.74 \pm 0.53) \times 10^{-13}$	$1.37^{+0.02}_{-0.02}$	$2.06^{+0.06}_{-0.06}$	1.26	0.39	$(9.30 \pm 1.81) \times 10^{-3}$
091127	9.69	$(9.95 \pm 1.65) \times 10^{-12}$	$1.53^{+0.02}_{-0.02}$	$1.71^{+0.05}_{-0.05}$	1.14	0.60	$(2.28 \pm 0.38) \times 10^{-1}$
100906A	9.68	$(2.52 \pm 0.55) \times 10^{-13}$	$1.99^{+0.04}_{-0.04}$	$1.97^{+0.07}_{-0.07}$	1.53	0.36	$(6.92 \pm 1.50) \times 10^{-3}$
101219B	10.45	$(4.58 \pm 0.91) \times 10^{-13}$	$0.65^{+0.03}_{-0.03}$	$2.16^{+0.15}_{-0.13}$	1.30	0.69	$(1.30 \pm 0.26) \times 10^{-2}$
110213A	11.19	$(6.97 \pm 1.83) \times 10^{-13}$	$1.93^{+0.04}_{-0.04}$	$1.98^{+0.05}_{-0.05}$	1.51	0.40	$(2.53 \pm 0.67) \times 10^{-2}$
111228A	11.03	$(2.56 \pm 0.67) \times 10^{-12}$	$1.14^{+0.02}_{-0.02}$	$1.94^{+0.05}_{-0.05}$	1.29	0.56	$(7.73 \pm 2.01) \times 10^{-2}$
120119A	11.58	$(4.75 \pm 0.94) \times 10^{-13}$	$1.89^{+0.11}_{-0.11} \dagger$	$1.73^{+0.07}_{-0.09}$	1.33	0.28	$(1.23 \pm 0.24) \times 10^{-2}$
120729A	6.57	$(3.49 \pm 0.96) \times 10^{-14}$	$2.96^{+0.17}_{-0.15}$	$2.08^{+0.22}_{-0.16}$	1.55	0.58	$(2.77 \pm 0.76) \times 10^{-4}$
120811C	5.87	$(4.36 \pm 1.07) \times 10^{-13}$	$1.19^{+0.09}_{-0.08}$	$2.12^{+0.13}_{-0.12}$	1.27	0.32	$(7.43 \pm 1.82) \times 10^{-3}$
121211A	7.90	$(9.59 \pm 1.82) \times 10^{-13}$	$1.30^{+0.18}_{-0.07}$	$1.83^{+0.15}_{-0.15}$	1.24	0.48	$(1.70 \pm 0.32) \times 10^{-2}$
130420A	11.39	$(6.38 \pm 1.68) \times 10^{-13}$	$1.14^{+0.04}_{-0.04}$	$2.07^{+0.12}_{-0.11}$	1.24	0.46	$(2.00 \pm 0.53) \times 10^{-2}$
140213A	10.76	$(4.09 \pm 0.81) \times 10^{-12}$	$0.99^{+0.02}_{-0.02}$	$1.86^{+0.04}_{-0.02}$	1.27	0.41	$(1.11 \pm 0.22) \times 10^{-1}$
140423A	11.91	$(2.04 \pm 0.53) \times 10^{-13}$	$1.49^{+0.10}_{-0.09}$	$1.94^{+0.15}_{-0.13}$	1.11	0.22	$(5.47 \pm 1.41) \times 10^{-3}$
140506A	11.77	$(3.12 \pm 0.83) \times 10^{-12}$	$0.98^{+0.02}_{-0.02}$	$1.87^{+0.06}_{-0.05}$	1.41	0.49	$(1.08 \pm 0.29) \times 10^{-1}$
140512A	10.38	$(6.48 \pm 1.17) \times 10^{-12}$	$1.67^{+0.05}_{-0.05}$	$1.88^{+0.05}_{-0.05}$	1.33	0.54	$(1.81 \pm 0.33) \times 10^{-1}$
140606B	37.22	$(6.16 \pm 1.25) \times 10^{-13}$	$0.90^{+0.43}_{-0.36}$	$1.90^{+0.55}_{-0.43}$	1.56	0.70	$(7.02 \pm 1.42) \times 10^{-2}$
140620A	11.39	$(7.68 \pm 2.02) \times 10^{-13}$	$1.53^{+0.10}_{-0.09}$	$2.00^{+0.15}_{-0.15}$	1.29	0.33	$(2.47 \pm 0.65) \times 10^{-2}$

GRB	$t_{x,\text{rest}}$ (h)	$F_x [0.3-10\text{keV}]$ ($\text{erg cm}^{-2} \text{ s}^{-1}$)	α_x	Γ_x	Absorption Correction	k	$F_{\nu,x} [5\text{keV}]$ (μJy)
140703A	5.29	$(3.01 \pm 0.49) \times 10^{-13}$	$1.74^{+0.10}_{-0.09}$	$1.90^{+0.09}_{-0.06}$	1.24	0.21	$(2.04 \pm 0.33) \times 10^{-3}$
140801A	15.09	$(1.41 \pm 0.36) \times 10^{-13}$	$0.92^{+0.15}_{-0.13}$	$1.80^{+0.36}_{-0.24}$	1.24	0.36	$(4.71 \pm 1.22) \times 10^{-3}$
140907A	10.44	$(9.94 \pm 1.99) \times 10^{-13}$	$1.05^{+0.11}_{-0.06}$	$1.98^{+0.10}_{-0.07}$	1.47	0.45	$(3.27 \pm 0.65) \times 10^{-2}$
141004A	4.14	$(1.87 \pm 0.33) \times 10^{-13}$	$1.14^{+0.03}_{-0.03}$	$1.79^{+0.13}_{-0.09}$	1.35	0.58	$(1.98 \pm 0.35) \times 10^{-3}$
150301B	7.76	$(1.49 \pm 0.57) \times 10^{-13}$	$1.11^{+0.03}_{-0.02}$	$1.81^{+0.09}_{-0.07}$	1.12	0.33	$(2.23 \pm 0.86) \times 10^{-3}$
150821A	6.67	$(8.36 \pm 1.75) \times 10^{-13}$	$1.33^{+0.05}_{-0.04}$	$2.44^{+0.14}_{-0.13}$	2.39	0.73	$(2.26 \pm 0.47) \times 10^{-2}$
151027A	9.76	$(2.65 \pm 0.62) \times 10^{-12}$	$1.85^{+0.07}_{-0.05}$	$2.08^{+0.13}_{-0.12}$	1.30	0.58	$(6.54 \pm 1.52) \times 10^{-2}$
160804A	11.94	$(7.63 \pm 1.26) \times 10^{-13}$	$0.92^{+0.06}_{-0.05}$	$1.97^{+0.12}_{-0.12}$	1.24	0.57	$(2.41 \pm 0.40) \times 10^{-2}$
161017A	10.57	$(3.70 \pm 0.84) \times 10^{-13}$	$1.80^{+0.10}_{-0.10}$	$1.87^{+0.12}_{-0.09}$	1.06	0.29	$(7.83 \pm 1.68) \times 10^{-3}$
170113A	10.86	$(7.74 \pm 1.86) \times 10^{-13}$	$1.20^{+0.02}_{-0.02}$	$1.78^{+0.05}_{-0.05}$	1.23	0.27	$(1.71 \pm 0.41) \times 10^{-2}$

Table 2. X-ray properties of the sample. F_x is in the range 0.3 – 10 keV in the observer frame. The absorption correction is the ratio of the counts-to-flux unabsorbed over the counts-to-flux observed from the spectrum on the UKSSDC. $F_{\nu,x}$ has been extrapolated to 11 hours and 5 keV in the rest frame, and has had a k-factor applied to account for the redshift of the observed bandpass. k is the ratio of the observer frame fluence to rest frame fluence, as in [Bloom et al. \(2001\)](#). All tabulated values are from the UKSSDC unless marked otherwise. [†]Manual fit. (1) - [Cano et al. \(2011\)](#)

2.3. Optical Data

Our optical data (Table 3) are collected from the literature, as well as GCN circulars. We select data that is as close to the rest-frame R-band as possible, which usually means the J, H or K nIR bands in the observer frame where available. We also aim to collect data as close to 11 hours in the rest frame as possible. Because optical/nIR coverage is never as comprehensive as it is for the X-ray, it is rarer to find values for the temporal, and in particular the spectral, indices in the literature. Where no published value exists, we fit light curves and SEDs from GCN circulars to provide our own values where possible. Light curves are fitted with both a single power law and a broken power law, which is assessed for an improvement in the fit using an f-test, and a break is accepted at the 3σ level. It is the index local to the observed data point that is reported in Table 3. SEDs are fitted with

a power law multiplied by the parameterised extinction curves of [Cardelli et al. \(1989\)](#). If the model does not converge when both the spectral index β_o and rest frame V-band extinction A_V are free parameters (usually due to a lack of nIR detections in the fitted SED), we fit the data with $\beta_o = \beta_x$ to account for the case where the synchrotron cooling break (ν_c) does not lie between the two bands, then fix $\beta_o = \beta_x - 0.5$ to account for the case where it does. We then report the extinction for the best fit, but do not report the spectral index, since this would effectively double-count β_x in our analysis.

We correct the magnitudes reported in the literature for galactic extinction using the maps from [Schlafly & Finkbeiner \(2011\)](#), and for intrinsic extinction where it can be identified. Magnitudes are then converted to flux densities and extrapolated from their observed wavelength to the rest frame R-band wavelength ($\lambda_{R,\text{rest}} = 6400 \times (1 + z)\text{\AA}$) using β_o , and to

11 h in the rest frame using α_o . In the absence of an SED or sufficient data for a light curve, we take the mean spectral and temporal indices from the sample of known values when extrapo-

lating to the desired time/frequency, and introduce the associated standard deviation into the uncertainty of the flux density. This is indicated by the bracketed values in Table 3.

GRB	$t_{o,rest}$ (h)	m	Filter	$A_{\lambda,obs}$ (Gal)	$A_{\lambda,rest}$ (Int)	β_o	α_o	$F_{\nu,o}$ (μJy)
LAT								
080916C	6.10	$21.10 \pm 0.15^{(1)}$	K_s (AB)	0.10	$0.00^{+0.00}_{-0.00}^{(1)}$	$0.38 \pm 0.20^{(1)}$	$1.40 \pm 0.05^{(1)}$	$7.55^{+1.04}_{-1.04}$
090323	10.82	$21.01 \pm 0.04^{(2)}$	R	0.05	$0.46^{+0.13}_{-0.10}^{(3)}$	$0.65 \pm 0.13^{(3)}$	$1.74 \pm 0.05^{(2)}$	$50.43^{+4.94}_{-6.38}$
090328A	22.12	$19.54 \pm 0.06^{(4)}$	J (AB)	0.04	$0.15^{+0.04}_{-0.12}^{(3)}$	$1.19 \pm 0.20^{(3)}$	$1.85 \pm 0.13^{(2)}$	$207.14^{+26.06}_{-13.85}$
090902B	12.16	$19.99 \pm 0.15^{(5)}$	J	0.03	$0.00^{+0.00}_{-0.00}^{(3)}$	$0.82 \pm 0.10^{(2)}$	$0.89 \pm 0.03^{(2)}$	$24.39^{+3.37}_{-3.37}$
090926A	9.35	$18.29 \pm 0.10^{(2)}$	I	0.04	$0.22^{+0.15}_{-0.15}$	0.94 ± 0.12	$1.63 \pm 0.01^{(6)}$	$244.43^{+25.17}_{-36.04}$
091003	21.38	$21.33 \pm 0.11^{(7)}$	r	0.05	-	(0.76 ± 0.29)	1.04 ± 0.05	$34.99^{+7.04}_{-7.04}$
091208B	7.44	$20.61 \pm 0.10^{(8)}$	J (AB)	0.04	$0.36^{+0.07}_{-0.07}$	(0.76 ± 0.29)	$0.75 \pm 0.02^{(9)}$	$23.14^{+2.58}_{-2.58}$
100414A	30.81	$20.9 \pm 0.1^{(10)}$	r'	0.05	-	$1.2 \pm 0.2^{(11)}$	$2.6 \pm 0.1^{(11)}$	$692.63^{+63.79}_{-63.79}$
100728A	2.90	$21.2 \pm 0.3^{(12)}$	H (AB)	0.09	-	(0.76 ± 0.29)	(1.22 ± 0.44)	$2.62^{+1.69}_{-1.69}$
110731A	17.17	$22.31 \pm 0.28^{(13)}$	H (AB)	0.09	$0.35^{+0.09}_{-0.09}^{(13)}$	$0.66 \pm 0.03^{(13)}$	1.08 ± 0.01	$13.90^{+3.76}_{-3.76}$
120711A	12.47	$19.74 \pm 0.27^{(14)}$	H (AB)	0.05	$0.68^{+0.05}_{-0.05}^{(14),a}$	$0.53 \pm 0.02^{(14)}$	1.25 ± 0.03	$103.60^{+26.17}_{-26.17}$
130427A	11.82	$16.99 \pm 0.03^{(15)}$	z	0.03	$0.10^{+0.05}_{-0.05}^{(15),b}$	$0.60 \pm 0.02^{(15)}$	$1.36 \pm 0.02^{(16)}$	$696.80^{+35.33}_{-35.33}$
130518A	12.86	$20.19 \pm 0.04^{(17)}$	i'	0.23	$0.04^{+0.08}_{-0.04}$	0.90 ± 0.07	1.33 ± 0.05	$122.60^{+6.39}_{-10.10}$
130907A	23.81	$21.38 \pm 0.09^{(18)}$	i	0.02	$2.18^{+0.17}_{-0.17}^{(19)}$	(0.76 ± 0.29)	$1.37 \pm 0.38^{(19)}$	$349.37^{+86.32}_{-86.32}$
131108A	4.31	$19.09 \pm 0.08^{(20)}$	H (AB)	0.02	$0.00^{+0.00}_{-0.00}$	0.86 ± 0.05	1.60 ± 0.07	$24.84^{+1.83}_{-1.83}$
131231A	12.72	$18.48 \pm 0.02^{(21)}$	R	0.05	-	(0.76 ± 0.29)	1.30 ± 0.04	$228.77^{+33.47}_{-33.47}$
141028A	11.81	$21.00 \pm 0.05^{(22)}$	r'	0.11	$0.00^{+0.00}_{-0.00}^{(23)}$	0.92 ± 0.04	$0.97 \pm 0.03^{(22)}$	$52.63^{+2.42}_{-2.42}$
150314A	5.74	$22.7 \pm 0.3^{(24)}$	R	0.08	-	(0.76 ± 0.29)	0.89 ± 0.13	$3.32^{+1.35}_{-1.35}$
150403A	3.53	$19.1 \pm 0.1^{(25)}$	r	0.13	-	(0.76 ± 0.29)	(1.22 ± 0.44)	$54.63^{+32.94}_{-32.94}$
150514A	16.07	$19.2 \pm 0.2^{(26)}$	J	0.02	$0.00^{+0.00}_{-0.00}$	(0.76 ± 0.29)	(1.22 ± 0.44)	$48.27^{+11.97}_{-11.97}$
160509A	11.39	$24.05 \pm 0.14^{(27)}$	r'	0.67	$6.85^{+0.16}_{-0.14}^{(28)}$	(0.76 ± 0.29)	$1.09 \pm 0.45^{(28)}$	$1678.07^{+496.44}_{-511.30}$
160623A	10.36	$20.32 \pm 0.13^{(29)}$	R	3.27	$1.32^{+0.03}_{-0.03}$	(0.76 ± 0.29)	1.29 ± 0.06	$1834.57^{+280.24}_{-280.24}$
160625B	14.66	$18.98 \pm 0.03^{(30)}$	H (AB)	0.06	$0.06^{+0.03}_{-0.03}$	0.47 ± 0.07	0.92 ± 0.01	$132.76^{+5.57}_{-5.57}$
GBM								
080916A	12.22	$22.1 \pm 0.07^{(31)}$	r'	0.05	-	(0.76 ± 0.29)	$0.81 \pm 0.13^{(31)}$	$9.01^{+1.54}_{-1.54}$
081007	9.89	$20.65 \pm 0.15^{(32)}$	r'	0.03	$0.46^{+0.37}_{-0.34}$	$0.43 \pm 0.36^{(33)}$	$1.25 \pm 0.13^{(32)}$	$33.14^{+11.38}_{-12.21}$
081121	1.54	$16.75 \pm 0.15^{(34)}$	K	0.01	$0.00^{+0.00}_{-0.00}$	0.42 ± 0.24	$1^{(34)} (\pm 0.44)$	$19.12^{+2.64}_{-2.64}$
090423	9.28	$20.58 \pm 0.06^{(35)}$	K	0.01	-	$0.30 \pm 0.06^{(35)}$	$1.36 \pm 0.33^{(35)}$	$4.24^{+0.23}_{-0.23}$

GRB	$t_{\text{o,rest}}$ (h)	m	Filter	$A_{\lambda,\text{obs}}$ (Gal)	$A_{\lambda,\text{rest}}$ (Int)	β_o	α_o	$F_{\nu,o}$ (μJy)
090424	9.79	$19.70 \pm 0.04^{(36)}$	I	0.04	$0.72^{+0.10}_{-0.10}$	0.89 ± 0.10	1.13 ± 0.03	$72.44^{+6.94}_{-6.94}$
090618	11.69	$19.36 \pm 0.01^{(37)}$	i	0.13	$0.29^{+0.11}_{-0.11}^{(37)}$	$0.55 \pm 0.07^{(37)}$	$1.57 \pm 0.07^{(37)}$	$119.74^{+12.04}_{-12.04}$
091020	14.52	$21.81 \pm 0.23^{(38)}$	R	0.05	$2.84^{+0.09}_{-0.27}^{(33)}$	(0.76 ± 0.29)	$1.12 \pm 0.06^{(39)}$	$240.80^{+105.35}_{-89.07}$
091127	10.95	$18.76 \pm 0.05^{(40)}$	i'	0.06	$0.12^{+0.05}_{-0.05}^{(40),c}$	$0.30 \pm 0.05^{(40)}$	$1.64 \pm 0.06^{(40)}$	$141.05^{+9.19}_{-9.19}$
100906A	13.11	$22.15 \pm 0.05^{(41)}$	R	0.81	$0.99^{+0.25}_{-0.25}^{(41),d}$	$1.34 \pm 0.04^{(41)}$	2.03 ± 0.02	$121.63^{+29.06}_{-29.06}$
101219B	6.96	$19.81 \pm 0.04^{(42*)}$	z'	0.02	-	$0.92 \pm 0.09^{(43)}$	$1.01 \pm 0.01^{(42)}$	$30.11^{+1.11}_{-1.11}$
110213A	10.05	$19.61 \pm 0.05^{(44)}$	i'	0.53	-	$1.22 \pm 0.18^{(44)}$	$1.80 \pm 0.15^{(44)}$	$166.99^{+7.69}_{-7.69}$
111228A	11.06	$20.3 \pm 0.1^{(45)}$	r'	0.08	$0.00^{+0.00}_{-0.00}^{(46)}$	$0.90 \pm 0.05^{(46)}$	1.04 ± 0.09	$49.13^{+4.52}_{-4.52}$
120119A	2.29	$17.14 \pm 0.24^{(47)}$	H	0.05	$0.81^{+0.01}_{-0.01}^{(46)}$	$0.89 \pm 0.01^{(47)}$	$1.30 \pm 0.01^{(47)}$	$44.02^{+9.74}_{-9.74}$
120729A	10.27	$23.27 \pm 0.27^{(48)}$	z'	0.20	$0.17^{+0.06}_{-0.06}^{(48)}$	$1.0 \pm 0.1^{(48)}$	$2.7 \pm 0.18^{(48)}$	$2.64^{+0.67}_{-0.67}$
120811C	7.39	$22.3 \pm 0.2^{(49)}$	R	0.08	-	(0.76 ± 0.29)	$1.04 \pm 0.05^{(49)}$	$7.02^{+2.97}_{-2.97}$
121211A	11.03	$22.1 \pm 0.4^{(50)}$	z	0.01	-	(0.76 ± 0.29)	1.18 ± 0.47	$6.94^{+2.66}_{-2.66}$
130420A	11.18	$20.38 \pm 0.23^{(51)}$	H (AB)	0.01	$0.07^{+0.02}_{-0.02}^{(52)}$	(0.76 ± 0.29)	0.95 ± 0.03	$26.23^{+5.61}_{-5.61}$
140213A	10.44	$18.6 \pm 0.1^{(53)}$	R	0.34	$0.00^{+0.00}_{-0.00}^{(54)}$	$0.8 \pm 0.1^{(54)}$	(1.22 ± 0.44)	$268.87^{+25.53}_{-25.53}$
140423A	10.99	$21.87 \pm 0.35^{(55)}$	H (AB)	0.01	-	0.73 ± 0.19	1.05 ± 0.02	$9.65^{+3.11}_{-3.11}$
140506A	30.75	$21.09 \pm 0.13^{(56)}$	J (AB)	0.21	$0.72^{+0.08}_{-0.08}^{(56),e}$	0.40 ± 0.38	0.60 ± 0.03	$57.11^{+8.03}_{-8.03}$
140512A	4.59	$19.0 \pm 0.1^{(57)}$	J (AB)	0.12	$0.00^{+0.00}_{-0.00}$	0.89 ± 0.09	(1.22 ± 0.44)	$31.16^{+12.27}_{-12.27}$
140606B	20.98	$21.30 \pm 0.11^{(58)}$	i	0.19	$0.46^{+0.08}_{-0.08}$	(0.76 ± 0.29)	$1.49 \pm 0.43^{(58)}$	$56.96^{+7.50}_{-7.50}$
140620A	13.82	$21.9 \pm 0.15^{(59)}$	R	0.13	-	(0.76 ± 0.29)	1.51 ± 0.17	$19.67^{+6.95}_{-6.95}$
140703A	2.49	$18.98 \pm 0.09^{(60)}$	H (AB)	0.02	$0.03^{+0.30}_{-0.03}^{(52)}$	(0.76 ± 0.29)	1.30 ± 0.16	$20.70^{+3.55}_{-6.71}$
140801A	6.52	$20.46 \pm 0.36^{(61)}$	H (AB)	0.12	$0.00^{+0.00}_{-0.00}^{(61)}$	$0.81 \pm 0.02^{(61)}$	$0.82 \pm 0.01^{(61)}$	$16.27^{+5.39}_{-5.39}$
140907A	10.97	$21.26 \pm 0.08^{(62)}$	R	0.65	-	(0.76 ± 0.29)	$1.2 \pm 0.1^{(63)}$	$31.76^{+7.73}_{-7.73}$
141004A	21.82	$23.4 \pm 0.2^{(64)}$	z	0.39	-	(0.74 ± 0.29)	1.08 ± 0.16	$5.13^{+0.96}_{-0.96}$
150301B	2.00	$20.6 \pm 0.4^{(65)}$	H (AB)	0.04	-	(0.76 ± 0.29)	(1.22 ± 0.44)	$2.72^{+2.27}_{-2.27}$
150821A	9.71	$22.0 \pm 0.2^{(66)}$	z	0.01	-	(0.76 ± 0.29)	(1.22 ± 0.44)	$5.85^{+1.18}_{-1.18}$
151027A	9.41	$16.4 \pm 0.1^{(67)}$	J	0.03	$0.00^{+0.00}_{-0.00}$	0.62 ± 0.07	1.89 ± 0.02	$320.42^{+29.51}_{-29.51}$
160804A	13.13	$20.20 \pm 0.07^{(68)}$	J (AB)	0.02	$0.06^{+0.11}_{-0.06}$	1.05 ± 0.23	1.54 ± 1.16	$37.43^{+3.18}_{-4.35}$
161017A	11.31	$19.80 \pm 0.03^{(69)}$	i	0.04	-	(0.76 ± 0.29)	1.46 ± 0.05	$92.78^{+24.37}_{-24.37}$
170113A	5.26	$20.8 \pm 0.3^{(70)}$	H (AB)	0.06	$0.00^{+0.00}_{-0.00}$	0.86 ± 0.17	0.94 ± 0.04	$10.63^{+2.94}_{-2.94}$

GRB	$t_{o,rest}$	m	Filter	$A_{\lambda,obs}$	$A_{\lambda,rest}$	β_o	α_o	$F_{\nu,o}$
	(h)			(Gal)	(Int)			(μ Jy)

Table 3. Optical/nIR properties of our sample. Lower case filters give magnitudes in the AB system. Upper case filters give Vega magnitudes unless otherwise indicated. Galactic extinction comes from [Schlafly & Finkbeiner \(2011\)](#). Intrinsic extinction uses an SMC-like extinction curve ($R_v = 2.74$) unless otherwise indicated. $F_{\nu,o}$ has been extrapolated to the rest frame R-band using the spectral index β_o , and to 11 h in the rest frame using the temporal index α_o . Bracketed values of α_o and β_o are the mean and standard deviation of the sample of known values. The standard deviation is introduced into the errors of $F_{\nu,o}$ when they are used. Results without references were calculated as part of this work.

(1) - [Greiner et al. \(2009\)](#); (2) - [Cenko et al. \(2011\)](#); (3) - [McBreen et al. \(2010\)](#); (4) - [Updike et al. \(2009a\)](#); (5) - [Pandey et al. \(2010\)](#); (6) - [Rau et al. \(2010\)](#); (7) - [Wiersema et al. \(2009a\)](#); (8) - [Updike et al. \(2009b\)](#); (9) - [Uehara et al. \(2012\)](#); (10) - [Filgas et al. \(2010\)](#); (11) - [Urata et al. \(2012\)](#); (12) - [Olivares et al. \(2010\)](#); (13) - [Ackermann et al. \(2013\)](#); (14) - [Martin-Carrillo et al. \(2014\)](#); (15) - [Perley et al. \(2014\)](#); (16) - [Maselli et al. \(2014\)](#); (17) - [Troja et al. \(2013a\)](#); (18) - [Butler et al. \(2013b\)](#); (19) - [Veres et al. \(2015\)](#); (20) - [Troja et al. \(2013b\)](#); (21) - [Halpern \(2014\)](#); (22) - [Cenko & Perley \(2014\)](#); (23) - [Graham et al. \(2014b\)](#); (24) - [Xu et al. \(2015\)](#); (25) - [Pugliese et al. \(2015\)](#); (26) - [Yates et al. \(2015\)](#); (27) - [Cenko et al. \(2016\)](#); (28) - [Laskar et al. \(2016\)](#); (29) - [Pozanenko et al. \(2016\)](#); (30) - [Watson et al. \(2016\)](#); (31) - [Rossi et al. \(2008\)](#); (32) - [Jin et al. \(2013\)](#); (33) - [Covino et al. \(2013\)](#); (34) - [Cobb \(2008\)](#); (35) - [Tanvir et al. \(2009\)](#); (36) - [Cobb \(2009\)](#); (37) - [Cano et al. \(2011\)](#); (38) - [Perley \(2009\)](#); (39) - [Kann et al. \(2009\)](#); (40) - [Troja et al. \(2012\)](#); (41) - [Gorbovskoy et al. \(2012\)](#); (42) - [Olivares et al. \(2015\)](#); (43) - [Sparre et al. \(2011\)](#); (44) - [Cucchiara et al. \(2011\)](#); (45) - [Cenko \(2011\)](#); (46) - [Nicuesa Guelbenzu et al. \(2011\)](#); (47) - [Morgan et al. \(2014\)](#); (48) - [Cano et al. \(2014\)](#); (49) - [Galeev et al. \(2012\)](#); (50) - [Butler et al. \(2012\)](#); (51) - [Butler et al. \(2013a\)](#); (52) - [Littlejohns et al. \(2015\)](#); (53) - [Trotter et al. \(2014\)](#); (54) - [Elliott et al. \(2014\)](#); (55) - [Butler et al. \(2014a\)](#); (56) - [Fynbo et al. \(2014b\)](#); (57) - [Graham et al. \(2014a\)](#); (58) - [Cano et al. \(2015\)](#); (59) - [Kelemen \(2014\)](#); (60) - [Butler et al. \(2014b\)](#); (61) - [Lipunov et al. \(2016\)](#); (62) - [Volnova et al. \(2014\)](#); (63) - [Cenko et al. \(2014\)](#); (64) - [Schmidl et al. \(2014\)](#); (65) - [Kann et al. \(2015\)](#); (66) - [Kruehler et al. \(2015\)](#); (67) - [Cano \(2015\)](#); (68) - [Bolmer & Greiner \(2016\)](#); (69) - [Guidorzi et al. \(2016\)](#); (70) - [Kruehler \(2017\)](#); a - $R_v = 3.41$; b - $R_v = 3$; c - $R_v = 3.3$; d - $R_v = 2.93$; e - $R_v = 3.1$; *we subtract out the extinction reported in [Olivares et al. \(2015\)](#).

2.4. Data Trends

The weighted mean of the X-ray temporal indices is 1.37 ± 0.24 and the weighted mean spectral index is 0.83 ± 0.11 . In the optical, the weighted mean temporal index is 1.14 ± 0.31 and the weighted mean spectral index is 0.79 ± 0.22 . The errors here are the weighted standard deviation, and the weights themselves are one over the errors squared. Bursts with temporal indices > 2 are excluded, as they indicate a jet break has occurred. Interpretation of these index distributions is complicated due to the different environment types and spectral regimes, but the spread in the temporal indices suggests

that we are seeing both ISM-like and wind-like GRBs, since the steeper end of the distribution is difficult to interpret as ISM-like due to the high value of p ($p \gtrsim 3$) implied by the relevant closure relations. Similarly, the shallower indices do not favor a wind-like environment, since the closure relations would require $p \ll 2$.

The distribution of $E_{\gamma,iso}$ for all GRBs in our sample is shown in Figure 1. We find a mean γ -ray energy of $E_{\gamma,iso} = 10^{53.46 \pm 0.54}$ ergs.

3. DETERMINING THE ENVIRONMENT TYPE

Our aim is to ascertain whether the X-ray and optical afterglow data are best described by

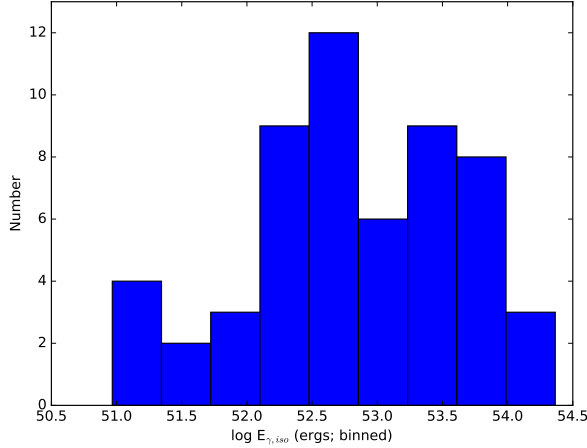


Figure 1. Histogram of the isotropic γ -ray energy release $E_{\gamma, \text{iso}}$ for all bursts in the sample. We find a mean γ -ray energy of $E_{\gamma, \text{iso}} = 10^{53.46 \pm 0.54}$ ergs.

deceleration in a wind-like medium or an ISM-like medium. To do this, we take our 4 power law measurements ($\alpha_x, \beta_x, \alpha_o, \beta_o$) and use the synchrotron closure relations to calculate the implied value of the electron distribution power law index p for each of the 5 possible scenarios, which are:

I $\nu_c < \nu_R < \nu_x$, where:

$$\alpha_o = \alpha_x = \frac{3p-2}{4}; \beta_o = \beta_x = \frac{p}{2}$$

(In this case, the synchrotron spectrum is identical in the observed regime for both wind and ISM, and the environment type cannot be determined)

II $\nu_R < \nu_c < \nu_x$ in an ISM-like environment, where:

$$\alpha_o = \frac{3(p-1)}{4}; \alpha_x = \frac{3p-2}{4}; \beta_o = \frac{p-1}{2}; \beta_x = \frac{p}{2}$$

III $\nu_R < \nu_c < \nu_x$ in a wind-like environment, where:

$$\alpha_o = \frac{3p-1}{4}; \alpha_x = \frac{3p-2}{4}; \beta_o = \frac{p-1}{2}; \beta_x = \frac{p}{2}$$

IV $\nu_R < \nu_x < \nu_c$ in an ISM-like environment, where:

$$\alpha_o = \alpha_x = \frac{3(p-1)}{4}; \beta_o = \beta_x = \frac{p-1}{2}$$

V $\nu_R < \nu_x < \nu_c$ in a wind-like environment, where:

$$\alpha_o = \alpha_x = \frac{3p-1}{4}; \beta_o = \beta_x = \frac{p-1}{2}$$

For scenarios I, IV and V, where ν_x and ν_R are on the same power law segment of the synchrotron spectrum, we can also use the calculated value of F_R/F_X as an indicator of p . Since $F_R = k\nu_R^{-\beta}$ and $F_X = k\nu_x^{-\beta}$, we find

$$F_R/F_X = (\nu_R/\nu_x)^{-\beta} = 2580^\beta, \quad (2)$$

where k is the normalisation constant and $\beta = (p-1)/2$ if $\nu_c > \nu_x$, or $\beta = p/2$ if $\nu_R > \nu_c$.

The electron distribution index p is assumed to be a single value for a given burst (Sari et al. 1998). We can therefore assess how well the values of p derived from each of our four or five different metrics converge in each environment type and spectral regime. Based on their agreement, we can assign probabilities to how likely each environment is for a given burst. To demonstrate the concept, we take an assumed value of $p = 2.5$ and tabulate the expected theoretical values of the spectral and temporal indices in the GRB afterglow for each environment type and spectral regime listed above (see Table 4).

When fitting to the data, we calculate the individual values of p from each measured index, and take the weighted mean of these as the best fit value for p . Our weights are $1/\text{errors}^2$. The error presented for p is the uncertainty of the weighted mean, rather than the standard deviation of the sample. The uncertainty of the weighted mean measures the dispersion of the mean of the sampling distribution around the mean of the population distribution. This provides an estimate of how well our value of p , derived from a limited sample, represents the true value of p , the mean of the overall population (i.e. the mean when $N = \infty$). We calculate χ_ν^2 (reduced χ^2), and assign probabilities that

$p = 2.5$	α_o	α_x	β_o	β_x
$\nu_c < \nu_R < \nu_x$	1.375	1.375	1.25	1.25
$\nu_R < \nu_c < \nu_x$ (ISM)	1.125	1.375	0.75	1.25
$\nu_R < \nu_c < \nu_x$ (wind)	1.625	1.375	0.75	1.25
$\nu_R < \nu_x < \nu_c$ (ISM)	1.125	1.125	0.75	0.75
$\nu_R < \nu_x < \nu_c$ (wind)	1.625	1.625	0.75	0.75

Table 4. The expected values of the afterglow spectral and temporal indices at X-ray and optical frequencies for an assumed $p = 2.5$ for each of the 5 cases outlined in Section 3.

each environment is the correct one by comparing the calculated χ^2_ν to the χ^2 distribution for the appropriate degrees of freedom.

Using this method, each burst is assigned a best-fit scenario and a best-fit value of p (with errors). An example using GRB 090424 is shown in Figure 2. We require that the best-fit p is consistent within 1 standard deviation with the range $1.8 \leq p \leq 3.0$. The best-fit scenario is accepted as the true environment type if the fit probability is at least 3 times better than the best fitting scenario of an alternative type that produces a value of p consistent with our accepted range. We make no minimum requirements on the *absolute* value of the probability an individual fit has, though the effects of using a minimum best-fit probability are discussed at the end of Section 5.3.

3.1. Constraining the Physical Parameters

Once we have identified the environment type and found a best-fit value of p for a burst, we are able to investigate the physical parameters underlying the emission.

For cases II and III, in which ν_c lies between the optical and X-ray bands, we can write (cf. Blandford & McKee 1976; Sari et al. 1998; Pe'er & Waxman 2005):

$$F_R/F_X = \left(\frac{\nu_R}{\nu_X} \right)^{-p/2} \nu_R^{1/2} \nu_c^{-1/2}. \quad (3)$$

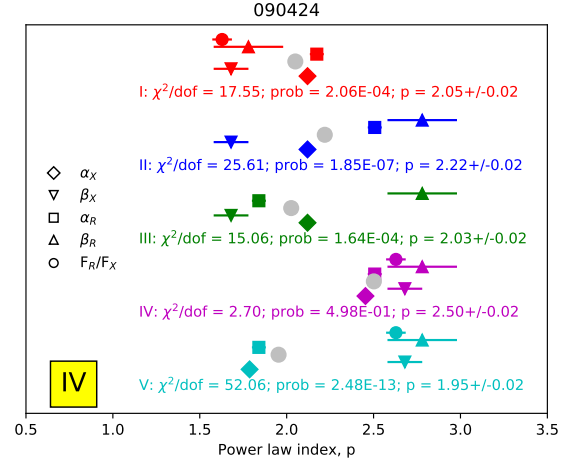


Figure 2. An example of our fitting procedure, using GRB 090424. Scenarios I-V are listed from top to bottom in different colors (see Table 4). Different symbols represent individual measures of p (i.e. temporal and spectral indices at X-ray and optical frequencies and F_R/F_X) with their 1σ errors. Grey circles represent the weighted mean of the data, taken as the best-fitting single value of p , and the errors are the uncertainty of the weighted mean (as opposed to the standard deviation of the data). Fit probabilities are derived by comparing reduced χ^2 to the χ^2 distribution for the appropriate degrees of freedom. Here, scenario IV ($\nu_R < \nu_x < \nu_c$; ISM) is the best fit because its probability is more than 3x better than the best fitting scenario of an alternate type. This is apparent in the clustering of the 5 data points when compared to the other scenarios.

We can gain information on the physical parameters of the shock from ν_c , which is

$$\nu_c = 5.6 \times 10^{13} \frac{1}{(1+Y)^2} \left(\frac{1+z}{2} \right)^{-1/2} \times E_{53}^{-1/2} t_{obs,day}^{-1/2} \epsilon_{B,-2}^{-3/2} n_0^{-1} \text{ Hz} \quad (4)$$

in the ISM case (case II), or

$$\nu_c = 3.7 \times 10^{13} \frac{1}{(1+Y)^2} \left(\frac{1+z}{2} \right)^{-3/2} \times E_{53}^{1/2} t_{obs,day}^{1/2} \epsilon_{B,-2}^{-3/2} A_*^{-2} \text{ Hz} \quad (5)$$

GRB	F_R/F_X	Environment type	Spectral regime	p	σ_p	SE_p	χ^2_ν	Probability
090323	$8944.11^{+2361.19}_{-2467.40}$	Wind	$\nu_R < \nu_c < \nu_x$	2.63	0.32	0.06	4.04	0.15
090328A	$3411.50^{+830.94}_{-745.62}$	ISM	$\nu_R < \nu_x < \nu_c$	3.15	0.25	0.05	2.75	0.49
090902B	707.87 ± 164.41	ISM	$\nu_R < \nu_c < \nu_x$	2.31	0.31	0.03	14.74	2.01×10^{-4}
090926A	$9640.05^{+2725.36}_{-2909.00}$	Wind	$\nu_R < \nu_c < \nu_x$	2.51	0.10	0.01	3.15	0.24
091003	804.33 ± 246.27	ISM	$\nu_R < \nu_x < \nu_c$	2.65	0.23	0.04	6.89	0.03
091208B	1145.25 ± 222.81	ISM	$\nu_R < \nu_c < \nu_x$	2.03	0.10	0.062	2.29	0.18
100728A	112.12 ± 77.24	Wind	$\nu_R < \nu_x < \nu_c$	2.43	0.13	0.04	1.31	0.38
110731A	1982.10 ± 765.28	ISM	$\nu_R < \nu_x < \nu_c$	2.53	0.14	0.01	23.14	8.10×10^{-6}
120711A	576.80 ± 195.34	Wind	$\nu_R < \nu_x < \nu_c$	2.44	0.31	0.01	50.74	5.52×10^{-13}
130427A	448.46 ± 104.13	Wind	$\nu_R < \nu_x < \nu_c$	2.15	0.15	0.01	20.38	4.04×10^{-5}
130907A	1798.34 ± 560.45	Wind	$\nu_R < \nu_x < \nu_c$	2.61	0.15	0.01	7.49	0.02
131108A	10294.02 ± 2495.61	Wind	$\nu_R < \nu_c < \nu_x$	2.48	0.19	0.04	2.96	0.27
131231A	586.77 ± 153.18	ISM	$\nu_R < \nu_x < \nu_c$	2.79	0.16	0.03	4.35	0.12
141028A	2591.39 ± 673.57	Unknown	$\nu_c < \nu_R < \nu_x$	1.95	0.09	0.03	0.83	0.90
150403A	591.93 ± 380.98	Wind	$\nu_R < \nu_x < \nu_c$	2.38	0.18	0.03	3.87	0.06
160623A	1216.66 ± 285.83	ISM	$\nu_R < \nu_x < \nu_c$	2.89	0.24	0.04	6.12	0.04
160625B	549.82 ± 125.94	ISM	$\nu_R < \nu_c < \nu_x$	2.23	0.11	0.01	6.84	0.03
GBM								
080916A	406.08 ± 111.96	ISM	$\nu_R < \nu_c < \nu_x$	2.29	0.13	0.06	0.56	0.66
081121	1076.56 ± 318.45	ISM	$\nu_R < \nu_x < \nu_c$	2.88	0.24	0.01	7.03	0.07
090424	565.49 ± 124.12	ISM	$\nu_R < \nu_x < \nu_c$	2.50	0.10	0.02	2.70	0.50
090618	593.57 ± 129.57	Wind	$\nu_R < \nu_x < \nu_c$	2.59	0.14	0.03	3.52	0.35
091127	619.13 ± 110.30	Wind	$\nu_R < \nu_x < \nu_c$	2.41	0.28	0.02	19.46	6.87×10^{-5}
100906A	17588.58 ± 5668.57	Unknown	$\nu_c < \nu_R < \nu_x$	2.50	0.31	0.05	7.03	0.01
101219B	2273.75 ± 460.45	Wind	$\nu_R < \nu_c < \nu_x$	1.67	0.22	0.01	14.96	8.31×10^{-4}
110213A	6587.84 ± 1756.07	Wind	$\nu_R < \nu_x < \nu_c$	3.02	0.22	0.04	4.10	0.27
111228A	635.51 ± 175.62	ISM	$\nu_R < \nu_x < \nu_c$	2.56	0.17	0.02	4.45	0.23
120119A	3584.06 ± 1063.29	ISM	$\nu_R < \nu_x < \nu_c$	2.76	0.12	0.01	11.12	0.01
120729A	9530.69 ± 3564.97	Unknown	$\nu_c < \nu_R < \nu_x$	2.28	0.23	0.08	0.89	0.51
130420A	1309.41 ± 444.11	ISM	$\nu_R < \nu_c < \nu_x$	2.24	0.06	0.03	0.54	0.67
140213A	2419.08 ± 529.16	Unknown	$\nu_c < \nu_R < \nu_x$	1.95	0.15	0.02	5.12	0.08
140506A	530.34 ± 158.82	ISM	$\nu_R < \nu_c < \nu_x$	1.91	0.13	0.02	3.90	0.16
140512A	172.39 ± 74.66	Wind	$\nu_R < \nu_x < \nu_c$	2.58	0.19	0.05	2.47	0.35

GRB	F_R/F_X	Environment type	Spectral regime	p	σ_p	SE_p	χ^2_ν	Probability
140703A	$10128.06^{+2388.19}_{-3668.34}$	ISM	$\nu_R < \nu_x < \nu_c$	3.23	0.31	0.06	4.37	0.12
140801A	3455.25 ± 1451.96	Unknown	$\nu_c < \nu_R < \nu_x$	1.75	0.13	0.01	4.38	0.24
150301B	1223.06 ± 1121.23	ISM	$\nu_R < \nu_x < \nu_c$	2.49	0.16	0.03	0.93	0.50
151027A	4900.49 ± 1227.01	Wind	$\nu_R < \nu_x < \nu_c$	2.88	0.25	0.02	9.28	0.02
170113A	621.81 ± 227.70	ISM	$\nu_R < \nu_x < \nu_c$	2.54	0.20	0.02	7.14	0.06

Table 5. The best fit results from trying to assign environment types to each GRB. Results tabulated here are at least a factor of three times better in probability than the next-best fit of an alternative environment type. σ_p is the weighted, unbiased sample standard deviation, representing the 1σ confidence interval of the sampling distribution. This error measures the spread of data points in the sample. SE_p is the uncertainty of the weighted mean (the standard error of the mean), representing the dispersion of the sample mean about the population mean. This error describes the uncertainty in our measured p (the sample mean) as an estimate of the true value of p (the population mean) due to the limited sample size.

The true standard error is estimated by investigating its effect on χ^2_ν and obtaining the maximum likelihood value. To do this, we take the χ^2_ν of each best fit and calculate its probability from the χ^2 probability density function with the relevant degrees of freedom. We then take the product of the probabilities for all 56 GRBs. This is done for all values of standard error in the range 0 to 0.5. We normalise the resulting function with its own integral via trapezium rule integration. Note that the probabilities used in this process are not the same as those used for identifying best fits, which are calculated using the χ^2 cumulative distribution function, rather than the χ^2 probability density function used here.

4. RESULTS

4.1. Identification of Environments

We are able to find a best fit with a probability at least three times greater than the best fit of an alternative environment type for 37 out of 56 GRBs (66 per cent). Of these, 14 (38 per cent) are best fitted with a wind-like environment, and 18 (49 per cent) with an ISM. We also find 5 bursts (14 per cent) that are best fit-

ted with $\nu_c < \nu_R$, and for these the environment type cannot be identified. The sum to 101 per cent is the result of rounding. We therefore find a nearly even split between wind-like and ISM-like bursts. Our results are displayed in Table 5. Our results generally agree with [Schulze et al. \(2011\)](#) where they overlap. The one exception is GRB 090926A, which we identify as wind-like.

For each best fit, we take the Gaussian probability density function with a mean of the measured value and standard deviation of the 1σ errors. We then take the sum of these distributions and normalise by the number of bursts to construct a maximum likelihood curve of p for our results, which is shown in Figure 3. Both wind and ISM-like bursts have a maximum likelihood $p \sim 2.5$, consistent with the findings of [Curran et al. \(2010\)](#), who showed that their sample of *Swift* GRBs exhibited values of p consistent with a Gaussian distribution centred at $p = 2.36$ with a width of 0.59. Bursts with $\nu_c < \nu_R$ have a maximum likelihood $p \sim 1.9$. The distribution with best fits three times better than the next best fit is highly similar to the overall distribution, indicating that this criterion is not biasing our results.

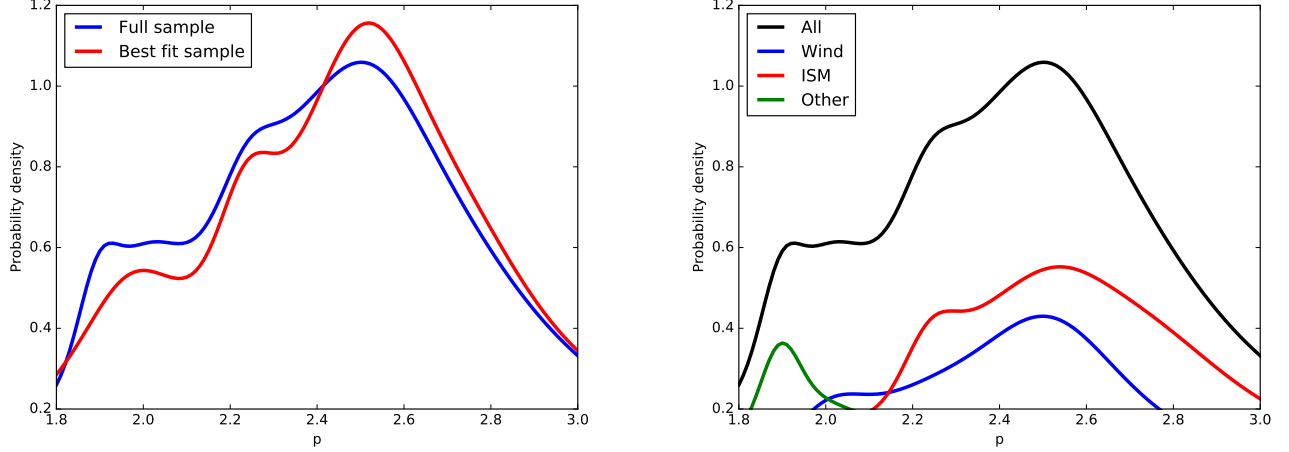


Figure 3. The maximum likelihood curve of the electron energy distribution power law index, p . This was found by summing the probability density functions for each best fit and normalising by the number of bursts.

Left: The distribution of the best fit sample (red), in which the best fitting model has to be at least three times higher in probability than the best fitting model of an alternate environment type. The distribution for all 56 GRBs is shown in blue. Both curves are normalised by the number of bursts they contain (37 and 56, respectively). The two distributions are highly similar.

Right: All 56 GRBs broken down into individual wind (blue), ISM (red) and $\nu_c < \nu_R$ (green) probability density functions. These curves are normalised by the total number of bursts (56). ISM and wind-like bursts share very similar probability density functions, with a most likely value of $p \sim 2.5$.

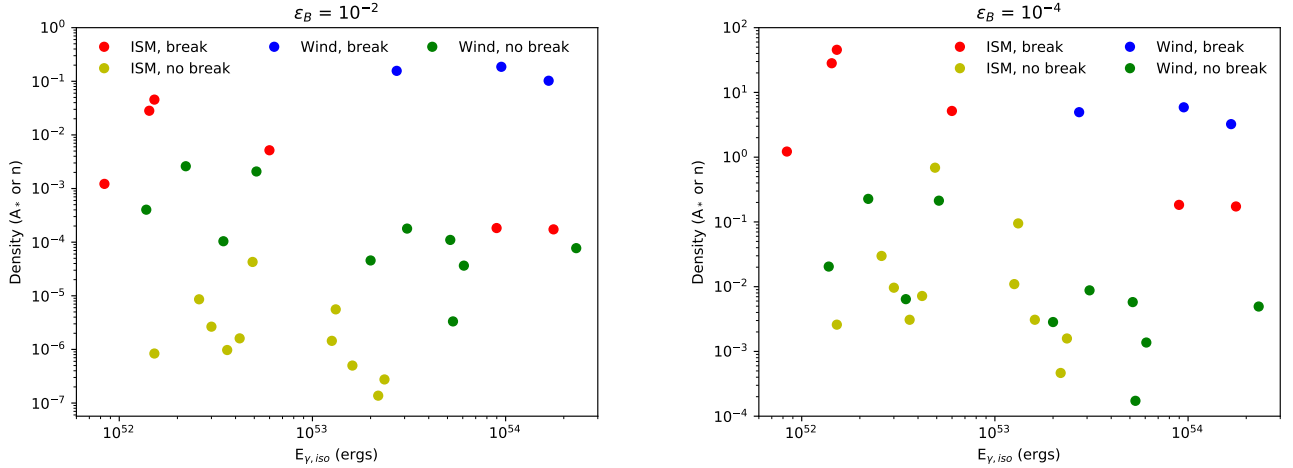


Figure 4. Estimates of environment density vs $E_{\gamma,iso}$ for an assumed value of ϵ_B and $\epsilon_e = 0.1$. Errors are found to be of a similar order of magnitude to the values. The units of the y-axis are mixed, and are cm^{-3} for the ISM-like bursts, or $5 \times 10^{11} \text{A}$ for wind-like bursts, where A is in g cm^{-1} . The left plot shows the inferred densities for $\epsilon_B = 10^{-2}$, and the right plot for $\epsilon_B = 10^{-4}$. Bursts in which $\nu_c < \nu_x$ are found to be in the densest environments, as would be expected. It is noticeable that $\epsilon_B = 10^{-2}$ leads to many ISM bursts having densities of just 10^{-6} cm^{-3} or lower, which is the intergalactic medium value. Lower values of ϵ_B are therefore favored.

4.2. Implications for the Blast-Wave

As discussed in Section 3.1, once the environment type is known and we have a measurement for p , we can solve the appropriate equation from Section 3.1 to find a value for the degenerate combination of ϵ_B and n (or A_*). In cases IV and V we must also assume a value for ϵ_e . Again, we take this value to be $\epsilon_e = 0.1$, following Beniamini & van der Horst (2017).

Figure 4 shows estimates of the density from two different assumed values of ϵ_B . We find that densities associated with $\epsilon_B = 10^{-2}$ are extremely low; in many cases 10^{-6} cm^{-3} or lower. Densities as low as this are associated with the intergalactic medium (IGM), and are therefore too low to be plausible around massive stars and in star forming regions. For this reason, lower values of ϵ_B are favored by our analysis, and we find $\epsilon_B = 10^{-4}$ gives a range of $10^{-4} < n < 10^2 \text{ cm}^{-3}$ and $10^{-3} < A_* < 10^1$. This finding suggests that $\epsilon_B = 10^{-2}$, which is commonly assumed in GRB literature, overestimates the magnetic field energy.

It is important to note that in our analysis, we use $E_{\gamma,iso}$ as a proxy for the total GRB energy. In fact, $E_{\gamma,iso}$ is the energy radiated by the electrons, and so ought to be $\sim \epsilon_e \times E_{tot}$. However, a large fraction of the prompt emission is likely to be thermal (at least in very high energy GRBs; Pe’er 2015), so our assumption is an acceptable estimate for the GRB energy.

Taking our density analysis a step further, we can use our results to estimate the emission radius and Lorentz factor of the shock front at a given time after trigger. Emission radius is given by

$$r = 5.85 \times 10^{17} \left(\frac{1+z}{2} \right)^{-1/4} E_{53}^{1/4} n_0^{-1/4} t_{day,obs}^{1/4} \text{ cm} \quad (8)$$

for the ISM and

$$r = 3.2 \times 10^{17} \left(\frac{1+z}{2} \right)^{-1/2} E_{53}^{1/2} A_*^{-1/2} t_{day,obs}^{1/2} \text{ cm} \quad (9)$$

for the wind. The Lorentz factor is given by

$$\Gamma = 10.6 \left(\frac{1+z}{2} \right)^{3/8} E_{53}^{1/8} n_0^{-1/8} t_{day,obs}^{-3/8} \quad (10)$$

in the ISM, and by

$$\Gamma = 11.1 \left(\frac{1+z}{2} \right)^{1/4} E_{53}^{1/4} A_*^{-1/4} t_{day,obs}^{-1/4} \quad (11)$$

for the wind (cf. Blandford & McKee 1976; Sari et al. 1998; Pe’er & Waxman 2005). Figure 5 shows the values for both at 11 hours after trigger in the rest frame. We use the densities implied for $\epsilon_B = 10^{-4}$. No clear separation is seen between the wind-like and ISM-like bursts in our sample, though the largest radii and highest Lorentz factors are all found in wind environments.

4.3. Intrinsic Error

As discussed in Section 3.2, we assume that the intrinsic error can be represented by an error in p , caused by the derived p not behaving as predicted by the standard power-law closure relations. The likelihood function for our estimate of the intrinsic error are plotted in Figure 6. We find a best estimate of the standard error of 0.25 ± 0.04 , or roughly a ten percent error given the typical value of p of 2.5.

4.4. Parameter Correlations

A number of measured parameters are available for correlative analysis: $E_{\gamma,iso}$, z , E_{peak} , F_R/F_X and T_{90} . In addition, we have the derived parameter p . We tested them against each other using the ranked Spearman correlation test (we use the Spearman test because it does not assume that the data are normally distributed). Firstly, we clearly recover the well-established correlation between $E_{\gamma,iso}$ and $E_{peak,rest}$ (Amati 2006) at a significance much greater than 3σ . We also see a correlation between $E_{\gamma,iso}$ and z at greater than 3σ significance. This is likely due to a selection effect in

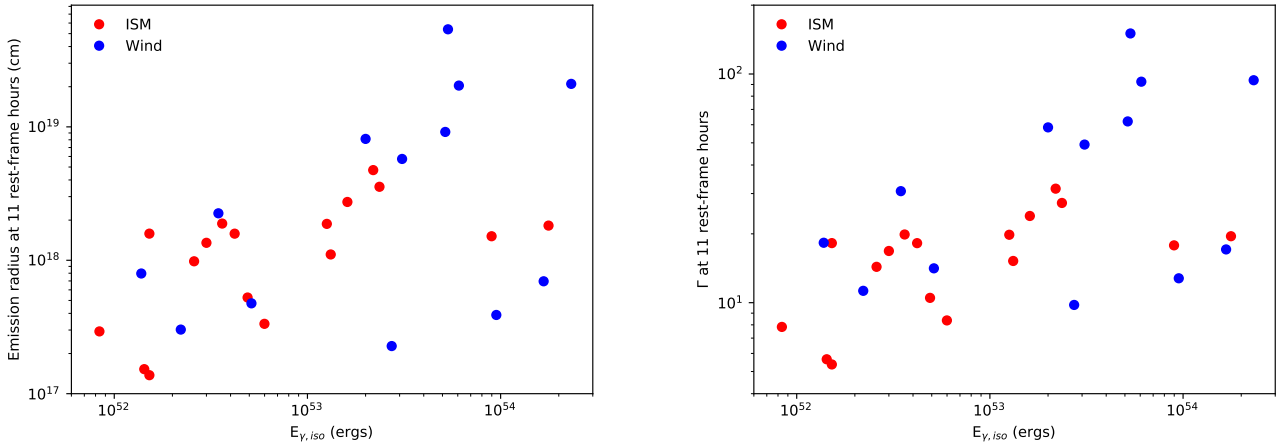


Figure 5. The estimated emission radius and Lorentz factor at 11 **hours rest-frame** after trigger. We assume $\epsilon_B = 10^{-4}$ and $\epsilon_e = 0.1$. The cluster of bursts in the upper right of the right panel have unusually high Lorentz factors for this time in the burst evolution. They reinforce the need for $\epsilon_B \ll 10^{-2}$, since lower assumed ϵ_B leads to lower implied Γ

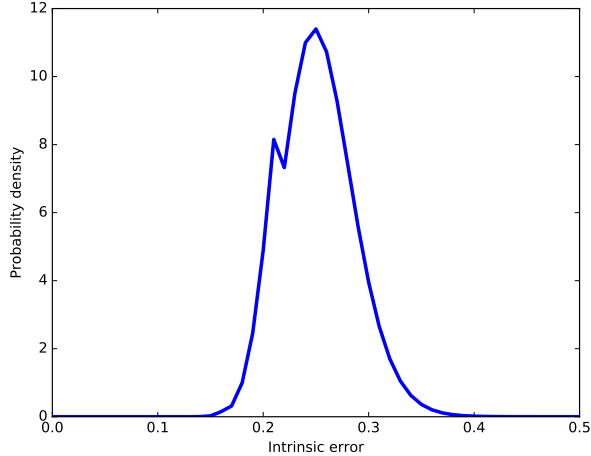


Figure 6. The normalised product of the best fit probabilities from the χ^2 probability density function for the 56 GRBs as a function of the standard error added in quadrature to the measured errors. The peak, indicating the maximum likelihood value, is at a standard error of 0.25 ± 0.04 .

which fainter bursts at greater distances do not trigger GRB satellites, so that the faint-distant population goes unobserved.

No other compelling correlations are seen between the data. There is a $> 3\sigma$ correlation be-

tween F_R/F_X and p , but only in the sample of wind-like bursts for which $\nu_c > \nu_x$. While this correlation is expected in this spectral regime because a higher F_R/F_X implies a steeper spectral index and therefore a greater value of p , the trend is not seen in the equivalent ISM sample, nor in the sample overall. In addition, the wind-like $\nu_c > \nu_x$ sub-sample contains only 11 GRBs. We also see a $> 3\sigma$ correlation between $E_{\gamma,iso}$ and rest-frame T_{90} for the 17 bursts that were designated ISM-like, but not in the wind-like bursts or the sample overall.

5. DISCUSSION

5.1. *Environments*

Through interpreting the synchrotron spectrum using the closure relations, as is standard in the field, we find a roughly equal split between wind-like and ISM-like environments within our population of GRBs. This raises the question of how these two distinct environments arise. There are two likely possibilities for this:

1. The two environments are due to two distinct progenitors.

2. Both originate from the same progenitor type, but are seen at different stages of evolution.

In practice these scenarios are not so different; a star with a weak stellar wind in the latter stages of life will influence its local environment to a lesser radial extent than a star with a strong stellar wind, so that an expanding jet from a GRB will cross into the ISM much faster as it will need to travel less distance. Since a more massive star is likely to release more energy on collapse, and also more likely to radiate a strong stellar wind, finding wind-like environments associated with more energetic GRBs perhaps makes intuitive sense. We tested this hypothesis by examining the cumulative distribution functions of $E_{\gamma, \text{iso}}$ for the bursts we identified as wind or ISM (Figure 7). Interestingly, we do indeed find a separation, with wind-like bursts typically exhibiting higher energies. A KS test reveals that this dichotomy is significant to 2σ , with a $p = 0.048$ probability that the two are drawn from the same overall population. However, since the test statistic falls short of 3σ significance, our finding is not fully conclusive. An increased sample size may help to confirm the result.

If the two types are from the same progenitor and we just observe them before/after they cross from a wind-like profile close to the parent star to an ISM-like profile beyond the termination shock, then it is reasonable to expect to see a number of cases where this transition is observed. Dai & Lu (2002) performed hydrodynamic simulations of GRB afterglows crossing a termination shock for ISM-ISM and wind-ISM transitions. Their results show that the expected signature is a sharp drop in the light curve, followed by a flare, then by the afterglow settling back into a power-law. For the wind-ISM transition, this second power-law is shallower than the pre-transition index. Such a signature has been claimed in a number of

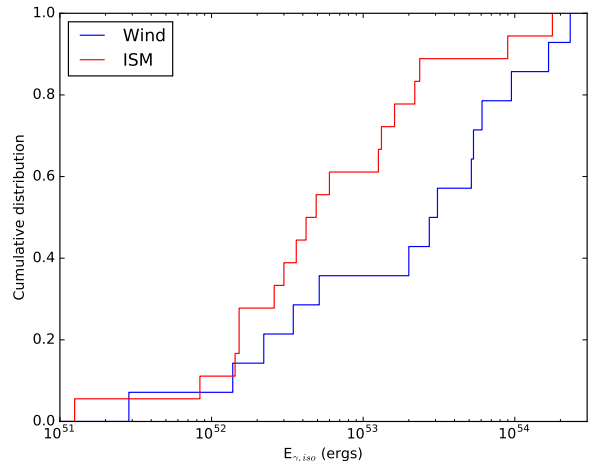


Figure 7. The cumulative distributions of the energies of bursts identified as being in wind-like (blue) or ISM-like (red) environments. The distributions do exhibit some separation, but a KS test finds a $p = 0.048$ probability that they are drawn from the same overall population, so any separation is not statistically significant above 2σ .

GRBs: 030226 (Dai & Wu 2003), 081109A (Jin et al. 2009), 080916C, 090902B, 090926A (Feng & Dai 2011) and 130907A (Veres et al. 2015). While suggestive, none of these are conclusive; in some cases the supposed transition occurs in gaps between the data, and in others the light curve behaviour could be explained by the transition between the prompt emission tail and the rise of the underlying afterglow, or the passage of ν_c through the X-ray bandpass.

The lack of identified termination shock crossings is concerning for a single LGRB progenitor scenario; previous studies of much smaller samples than ours (e.g. Panaitescu & Kumar 2002; Starling et al. 2008; Curran et al. 2009) find that 25 - 50 per cent of GRBs exhibit ISM-like environments (consistent with our own findings), and so termination shocks should be common, yet none are seen. We note that since we find a roughly even wind/ISM split when searching close to 11 rest-frame hours after trigger, this must be close to the mean termination shock

crossing time if this is the cause for the two observed environment types. However, while we may be close to the mean value, the spread of termination shock radii is likely to be quite high, perhaps deviating by as much as an order of magnitude (Pe'er & Wijers 2006).

5.2. Constraints on the Plasma Parameters

Our estimates of the local density in Figure 4 show that bursts with $\nu_c < \nu_x$ are found in the highest density environments. This is an expected result, since the frequency of ν_c is inversely proportional to density in the ISM (Equation 4), or the square of the density in a wind (Equation 5). Higher densities therefore more readily lead to $\nu_c < \nu_x$.

For similar progenitors, we may expect the emission radius to be higher for the ISM-like bursts, since these are supposed to be post-termination shock. However, Figure 5 shows that this is not the case for our sample; the highest inferred emission radii are all for wind-like media. This finding is consistent with the idea that the energy release and/or local density varies several orders of magnitudes in LGRBs. If the progenitors are the same for wind and ISM (i.e. emit a wind of a comparable strength), then the local environment density will determine the radial extent to which this stellar wind exerts influence. Following this, variations in the explosion energy determine how long it takes the forward shock to cross this region. If the progenitors are not the same, then this is further complicated by the varying wind strengths. Finding wind-like environments with larger emission radii and Lorentz factors than are found for the ISM-like environments tells us that the wind does not look the same in all LGRBs (Pe'er & Wijers 2006; van Marle et al. 2006).

We note that the cluster of bursts in the upper-right of the right-hand panel in Figure 5 have very high Lorentz factors for 11 hours after trigger. They are GRB 090323 ($\Gamma = 150$),

GRB 090926A ($\Gamma = 94$) and GRB 090902B ($\Gamma = 93$). The same bursts are also seen in the lower-right of the right-hand panel of Figure 4 in green. They have high measured $E_{\gamma,iso}$ and were found to have low densities. The implication is that their jets were launched with a high Lorentz factor, and the tenuous surrounding environment did little to slow them down. However, converting their inferred A_* to n at 11 hours after trigger reveals particle densities in the range $10^{-8} < n < 10^{-5} \text{ cm}^{-3}$, which is extremely low. This can potentially be alleviated by a lower ϵ_B , and further reinforces our earlier finding that $\epsilon_B \ll 10^{-2}$.

5.3. The Effects of Intrinsic Error

While our findings hold under a standard analysis of the GRB afterglows, we note a lack of success in fitting those GRBs with the most precise spectral and temporal index measurements. In these cases, the indicators of the underlying electron energy distribution, p , do not agree on a single value within their own errors. As discussed in Section 3.2, this may indicate complexity in nature that goes beyond the simple equivalence drawn between the measured indices and p through the closure relations. This intrinsic error may go unnoticed when the measured errors are large, but cause a falloff in goodness-of-fit with increasing precision. It is already known that standard synchrotron theory is a simplified model of a complex system, and it has been previously noted in the literature that the theory does not always do well against observations of GRB afterglows (e.g. Wang et al. 2015).

Figure 8 illustrates the difference adding a standard error makes using GRB 160625B. This burst had very high precision measurements of both the X-ray and r-band temporal indices, and as a result the best fit must stick very close to them. However, their slight disagreement with one another, and more pronounced disagreement with other indicators of p , means

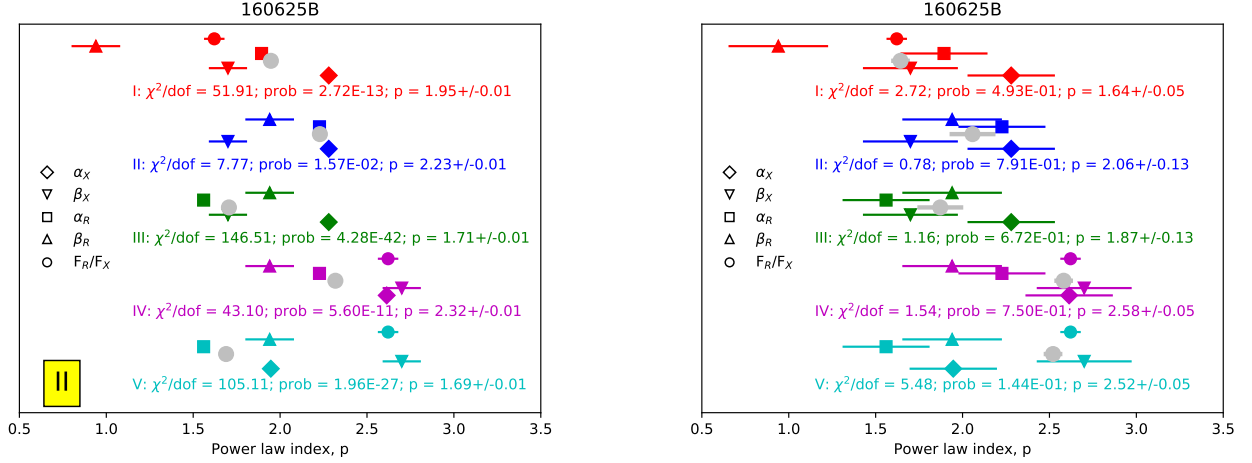


Figure 8. Fits for each of the 5 spectral regimes listed in Section 3. The measured values of α_x , β_x , α_o , β_o and F_R/F_X have been converted to p using the relevant closure relations, and the best fitting value of p is shown in grey for each spectral regime. The error on p is the uncertainty of the weighted mean, not the standard deviation of the data.

Left: Best fits with no added intrinsic error. Model II ($\nu_R < \nu_c < \nu_X$ in an ISM environment) is the best fit. However, with $\chi^2_\nu = 7.77$, it is not a good fit.

Right: Best fits with an intrinsic error of 0.25 added in quadrature to the measured errors for each index (except F_R/F_X). Model II is still the best fit, now with $\chi^2_\nu = 0.78$, but is no longer a factor of three times higher in probability than the best fit of an alternative environment type (model III; $\nu_R < \nu_c < \nu_X$ in a wind environment). Therefore, although an ISM is favored, we cannot say with certainty which environment surrounds GRB 160625B.

that this “best” fit had a $\chi^2_\nu = 7.77$; too high to be considered a good fit. With the standard error included, the best fit has a $\chi^2_\nu = 0.78$, but the most likely model is now not more than three times better than its nearest competitor of a different environment type. Losing definite best fits is an inevitable side effect of increasing the intrinsic error. An intrinsic error of 0.25 reduces the number of GRBs with identifiable best fit environments to 7 (down from 37). 2 wind environments, 1 ISM environment and 4 bursts where $\nu_c < \nu_R$ remain. The persistence of this last type is due to the fact that they occupy a niche by requiring steep optical spectral indices, whereas the other spectral regimes are more uniform in terms of their manifestations in the indices and so are easily confused with one another. They therefore more readily fall short of the requirement of being three times more probable than the next best fit. The number

of identifiable best fits as a function of intrinsic error is shown in Figure 9.

Ours is the first attempt to measure this uncertainty through the data, and we find that an intrinsic error of 0.25 ± 0.04 (about 10 per cent of p) added in quadrature is required to maximise the likelihood of the χ^2 probability density function of our results. Worryingly, this intrinsic error negates our ability to identify the environment type in almost all cases - a result that has sweeping consequences across the field if true. However, Table 5 shows that even without this intrinsic error, the majority of bursts do find acceptable best fits. Additionally, when a minimum best-fit probability is imposed on the sample (not including intrinsic error), the split between wind and ISM-like bursts remains constant. This was true for all minimum best-fit probabilities tested, from 10^{-12} up to 0.01 in order of magnitude increments.

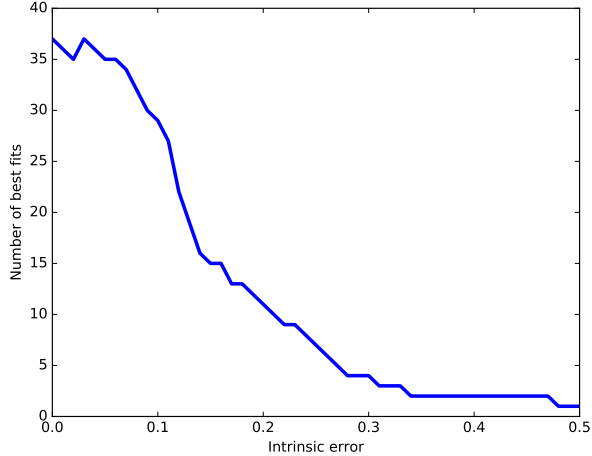


Figure 9. The number of surviving best fits (where the fit probability is at least three times better than the best fit of an opposing environment type) as a function of the added intrinsic error.

The leading candidates for the source of any intrinsic error are ongoing energy injection, Compton scattering, varying microphysical parameters, or deviations of the electron energy distribution from a power-law.

6. CONCLUSIONS

We have assessed the environments of a large sample of *Fermi* detected LGRBs by fitting their spectral and temporal indices with the synchrotron closure relations. We find a roughly even split between wind-like and ISM-like environments in cases where an environment could be assigned a fit probability at least three times higher than the next-best fit probability for an environment of a different type. This division persists when our factor three constraint is lessened, or when a minimum best-fit probability is imposed. The identification of two environment types indicates that either we see a single population of LGRBs before and after their forward shock emission sites have transitioned across a termination shock at the edge of a stellar wind-dominated bubble into the ISM, or that LGRBs are in fact the product of two distinct progenitors that occur in different environments.

If the two environment types are due to the crossing of the termination shock, then our chosen observation time of 11 hours in the rest-frame must be quite close to the mean shock crossing time, based on the roughly even division between wind (pre-crossing) and ISM (post-crossing) environments measured. However, we find a 2σ separation in the distributions of γ -ray isotropic equivalent energies between bursts identified as being in wind environments and those identified as being in ISM environments, with the wind bursts being systematically more energetic. This could be evidence for two distinct populations, though a larger sample will be required to make this claim with confidence.

Having identified the environment types and a best-fit value for p , we are able to analyze the physical parameters of the shock. Our results provide a value for the degenerate values of $\epsilon_B \times n$ (or A_*), though in some cases we must assume $\epsilon_e = 0.1$. The densities inferred by different values of assumed ϵ_B indicate that ϵ_B must be very low; $\epsilon_B \sim 10^{-4}$ or lower is required to avoid densities as sparse as the IGM, or unnaturally high Lorentz factors.

Finally, we find that those GRBs with the most precise measurements of their spectral and temporal indices (i.e. those with the smallest error bars) do not result in more precise convergences of these indices to a single value of an underlying power-law distribution of electron energies, as is typically assumed in synchrotron theory. This strongly indicates an intrinsic error in the GRB population that must be accounted for when assigning environment types using the closure relations. Our best fit value for this error is 0.25 ± 0.04 , obtained by maximising the likelihood of all the fits in our sample across a range of consistent intrinsic errors added in quadrature to the measured errors. This is the first measurement of the discrepancy between theory and nature made from the data. With

the intrinsic error included, our ability to determine the GRB environment type to a threshold of a factor of three in probability is diminished, but we nonetheless retain a roughly even split in wind/ISM best fits with/without this condition applied.

7. ACKNOWLEDGEMENTS

We thank David Rubin for an independent check of the intrinsic error presented in this pa-

per. BPG has received funding from the European Research Council (ERC) under the European Union’s Horizon 2020 research and innovation programme (grant agreement no 725246, TEDE, PI A. Levan). AP acknowledges support by the European Union Seventh Framework Program (FP7/2007-2013) under grant agreement no. 618499. This work made use of data supplied by the UK Swift Science Data Centre at the University of Leicester.

REFERENCES

- Ackermann, M., Ajello, M., Asano, K., et al. 2013, *ApJ*, 763, 71
- Amati, L. 2006, *MNRAS*, 372, 233
- Atwood, W. B., Abdo, A. A., Ackermann, M., et al. 2009, *ApJ*, 697, 1071
- Band, D., Matteson, J., Ford, L., et al. 1993, *ApJ*, 413, 281
- Beniamini, P., & van der Horst, A. J. 2017, *MNRAS*, 472, 3161
- Berger, E., Fox, D. B., Cucchiara, A., & Cenko, S. B. 2008, GRB Coordinates Network, 8335
- Berger, E., & Rauch, M. 2008, GRB Coordinates Network, 8542
- Bissaldi, E., McBreen, S., & Connaughton, V. 2008, GRB Coordinates Network, 8369
- Blandford, R. D., & McKee, C. F. 1976, *Physics of Fluids*, 19, 1130
- Bloom, J. S., Frail, D. A., & Sari, R. 2001, *AJ*, 121, 2879
- Bolmer, J., & Greiner, J. 2016, GRB Coordinates Network, 19774
- Butler, N., Watson, A. M., Kutyrev, A., et al. 2012, GRB Coordinates Network, 14077
- . 2013a, GRB Coordinates Network, 14431
- . 2013b, GRB Coordinates Network, 15208
- . 2014a, GRB Coordinates Network, 16174
- . 2014b, GRB Coordinates Network, 16513
- Cano, Z. 2013, *MNRAS*, 434, 1098
- . 2015, GRB Coordinates Network, 18552
- Cano, Z., Bersier, D., Guidorzi, C., et al. 2011, *MNRAS*, 413, 669
- Cano, Z., de Ugarte Postigo, A., Pozanenko, A., et al. 2014, *A&A*, 568, A19
- Cano, Z., de Ugarte Postigo, A., Perley, D., et al. 2015, *MNRAS*, 452, 1535
- Cardelli, J. A., Clayton, G. C., & Mathis, J. S. 1989, *ApJ*, 345, 245
- Castro-Tirado, A. J., Gorosabel, J., & Garcia-Rodriguez, A. 2014a, GRB Coordinates Network, 16797
- Castro-Tirado, A. J., Cunniffe, R., Sanchez-Ramirez, R., et al. 2014b, GRB Coordinates Network, 16505
- Cenko, S. B. 2011, GRB Coordinates Network, 12771
- Cenko, S. B., Cucchiara, A., Capone, J., et al. 2014, GRB Coordinates Network, 16818
- Cenko, S. B., & Perley, D. A. 2014, GRB Coordinates Network, 16989
- Cenko, S. B., Perley, D. A., Junkkarinen, V., et al. 2009, GRB Coordinates Network, 9518
- Cenko, S. B., Troja, E., & Tegler, S. 2016, GRB Coordinates Network, 19416
- Cenko, S. B., Frail, D. A., Harrison, F. A., et al. 2011, *ApJ*, 732, 29
- Chevalier, R. A., & Li, Z.-Y. 1999, *ApJL*, 520, L29
- . 2000, *ApJ*, 536, 195
- Chornock, R., Perley, D. A., Cenko, S. B., & Bloom, J. S. 2009, GRB Coordinates Network, 9243
- Cobb, B. E. 2008, GRB Coordinates Network, 8547
- . 2009, GRB Coordinates Network, 9313
- Covino, S., Melandri, A., Salvaterra, R., et al. 2013, *MNRAS*, 432, 1231
- Cucchiara, A., Fox, D., Levan, A., & Tanvir, N. 2009a, GRB Coordinates Network, 10202
- Cucchiara, A., & Fox, D. B. 2010, GRB Coordinates Network, 10606

- Cucchiara, A., Fox, D. B., Cenko, S. B., Tanvir, N., & Berger, E. 2009b, GRB Coordinates Network, 10031
- Cucchiara, A., & Prochaska, J. X. 2012, GRB Coordinates Network, 12865
- Cucchiara, A., Cenko, S. B., Bloom, J. S., et al. 2011, *ApJ*, 743, 154
- Curran, P. A., Evans, P. A., de Pasquale, M., Page, M. J., & van der Horst, A. J. 2010, *ApJL*, 716, L135
- Curran, P. A., Starling, R. L. C., van der Horst, A. J., & Wijers, R. A. M. J. 2009, *MNRAS*, 395, 580
- Dai, Z. G., & Lu, T. 2002, *ApJL*, 565, L87
- Dai, Z. G., & Wu, X. F. 2003, *ApJL*, 591, L21
- de Ugarte Postigo, A., Gorosabel, J., Thoene, C. C., et al. 2014a, GRB Coordinates Network, 16657
- de Ugarte Postigo, A., Kruehler, T., Flores, H., & Fynbo, J. P. U. 2015a, GRB Coordinates Network, 17523
- de Ugarte Postigo, A., Tanvir, N., Sanchez-Ramirez, R., et al. 2013a, GRB Coordinates Network, 14437
- de Ugarte Postigo, A., Thoene, C. C., Gorosabel, J., et al. 2013b, GRB Coordinates Network, 15470
- de Ugarte Postigo, A., Xu, D., Malesani, D., et al. 2013c, GRB Coordinates Network, 15187
- de Ugarte Postigo, A., Xu, D., Malesani, D., & Tanvir, N. R. 2015b, GRB Coordinates Network, 17822
- de Ugarte Postigo, A., Goldoni, P., Milvang-Jensen, B., et al. 2011, GRB Coordinates Network, 11579
- de Ugarte Postigo, A., Gorosabel, J., Xu, D., et al. 2014b, GRB Coordinates Network, 16310
- de Ugarte Postigo, A., Thoene, C. C., Malesani, D., et al. 2014c, GRB Coordinates Network, 16902
- de Ugarte Postigo, A., Fynbo, J. P. U., Thoene, C., et al. 2015c, GRB Coordinates Network, 17583
- de Ugarte Postigo, A., Kann, D. A., Thoene, C., et al. 2016, GRB Coordinates Network, 20069
- D'Elia, V., Fynbo, J. P. U., Covino, S., et al. 2010, *A&A*, 523, A36
- D'Elia, V., Kruehler, T., Wiersema, K., et al. 2015, GRB Coordinates Network, 18187
- Dittmann, J., Laskar, T., & Berger, E. 2011, GRB Coordinates Network, 12759
- Drenkhahn, G., & Spruit, H. C. 2002, *A&A*, 391, 1141
- Elliott, J., Varela, K., Kann, D. A., & Greiner, J. 2014, GRB Coordinates Network, 15829
- Evans, P. A., Beardmore, A. P., Page, K. L., et al. 2007, *A&A*, 469, 379
- . 2009, *MNRAS*, 397, 1177
- Feng, S.-Y., & Dai, Z.-G. 2011, *Research in Astronomy and Astrophysics*, 11, 1046
- Filgas, R., Kruehler, T., & Greiner, J. 2010, GRB Coordinates Network, 10607
- Fruchter, A. S., Levan, A. J., Strolger, L., et al. 2006, *Nature*, 441, 463
- Fynbo, J. P. U., Malesani, D., Hjorth, J., Sollerman, J., & Thoene, C. C. 2008, GRB Coordinates Network, 8254
- Fynbo, J. P. U., Tanvir, N. R., Jakobsson, P., et al. 2014a, GRB Coordinates Network, 16217
- Fynbo, J. P. U., Kruehler, T., Leighly, K., et al. 2014b, *A&A*, 572, A12
- Galeev, A., Khamitov, I., Bikmaev, I., et al. 2012, GRB Coordinates Network, 13636
- Gao, H., Lei, W.-H., Zou, Y.-C., Wu, X.-F., & Zhang, B. 2013, *NewAR*, 57, 141
- Gehrels, N., Barthelmy, S. D., Burrows, D. N., et al. 2008, *ApJ*, 689, 1161
- Golenetskii, S., Aptekar, R., Frederiks, D., et al. 2013, GRB Coordinates Network, 15203
- Gorbovskoy, E. S., Lipunova, G. V., Lipunov, V. M., et al. 2012, *MNRAS*, 421, 1874
- Graham, J., Varela, K., Delvaux, C., & Greiner, J. 2014a, GRB Coordinates Network, 16257
- Graham, J. F., Kann, D. A., Schady, P., & Greiner, J. 2014b, GRB Coordinates Network, 16977
- Granot, J., Panaitescu, A., Kumar, P., & Woosley, S. E. 2002, *ApJL*, 570, L61
- Greiner, J., Clemens, C., Kruehler, T., et al. 2009, *A&A*, 498, 89
- Gruber, D., Goldstein, A., Weller von Ahlefeld, V., et al. 2014, *ApJS*, 211, 12
- Guidorzi, C., Kobayashi, S., Steele, I. A., et al. 2016, GRB Coordinates Network, 20080
- Halpern, J. P. 2014, GRB Coordinates Network, 15646
- Hjorth, J., Sollerman, J., Møller, P., et al. 2003, *Nature*, 423, 847

- Jin, Z. P., Xu, D., Covino, S., et al. 2009, *MNRAS*, 400, 1829
- Jin, Z.-P., Covino, S., Della Valle, M., et al. 2013, *ApJ*, 774, 114
- Kann, D. A., Delvaux, C., & Greiner, J. 2015, GRB Coordinates Network, 17522
- Kann, D. A., Laux, U., Roeder, M., & Meusinger, H. 2009, GRB Coordinates Network, 10076
- Kasliwal, M. M., Cenko, S. B., & Singer, L. P. 2014, GRB Coordinates Network, 16425
- Kelemen, J. 2014, GRB Coordinates Network, 16440
- Kruehler, T. 2017, GRB Coordinates Network, 20457
- Kruehler, T., Schrey, F., Bornemann, W., Rau, A., & Greiner, J. 2015, GRB Coordinates Network, 18195
- Krühler, T., Malesani, D., Fynbo, J. P. U., et al. 2015, *A&A*, 581, A125
- Laskar, T., Alexander, K. D., Berger, E., et al. 2016, *ApJ*, 833, 88
- Levan, A. J., Tanvir, N. R., Fruchter, A. S., et al. 2014, *ApJ*, 792, 115
- Levesque, E. M., Kewley, L. J., Graham, J. F., & Fruchter, A. S. 2010, *ApJL*, 712, L26
- Li, L., Wu, X.-F., Huang, Y.-F., et al. 2015, *ApJ*, 805, 13
- Lipunov, V. M., Gorosabel, J., Pruzhinskaya, M. V., et al. 2016, *MNRAS*, 455, 712
- Littlejohns, O. M., Butler, N. R., Cucchiara, A., et al. 2015, *MNRAS*, 449, 2919
- Malesani, D., de Ugarte Postigo, A., de Pasquale, M., et al. 2016, GRB Coordinates Network, 19708
- Martin-Carrillo, A., Hanlon, L., Topinka, M., et al. 2014, *A&A*, 567, A84
- Maselli, A., Melandri, A., Nava, L., et al. 2014, *Science*, 343, 48
- McBreen, S., Krühler, T., Rau, A., et al. 2010, *A&A*, 516, A71
- Meegan, C., Lichti, G., Bhat, P. N., et al. 2009, *ApJ*, 702, 791
- Milne, P. A., & Cenko, S. B. 2011, GRB Coordinates Network, 11708
- Morgan, A. N., Perley, D. A., Cenko, S. B., et al. 2014, *MNRAS*, 440, 1810
- Narayana Bhat, P., Meegan, C. A., von Kienlin, A., et al. 2016, *ApJS*, 223, 28
- Nicuesa Guelbenzu, A., Klose, S., & Greiner, J. 2011, GRB Coordinates Network, 12757
- Oates, S. R., Page, M. J., De Pasquale, M., et al. 2012, *MNRAS*, 426, L86
- Oates, S. R., Racusin, J. L., De Pasquale, M., et al. 2015, *MNRAS*, 453, 4121
- Olivares, E. F., Kruehler, T., Filgas, R., et al. 2010, GRB Coordinates Network, 11020
- Olivares, E. F., Greiner, J., Schady, P., et al. 2015, *A&A*, 577, A44
- Paczynski, B. 1986, *ApJL*, 308, L43
- Panaitescu, A., & Kumar, P. 2001, *ApJ*, 554, 667
- . 2002, *ApJ*, 571, 779
- Pandey, S. B., Swenson, C. A., Perley, D. A., et al. 2010, *ApJ*, 714, 799
- Pe’er, A. 2015, *Advances in Astronomy*, 2015, 907321
- Pe’er, A., & Waxman, E. 2005, *ApJ*, 633, 1018
- Pe’er, A., & Wijers, R. A. M. J. 2006, *ApJ*, 643, 1036
- Perley, D. A. 2009, GRB Coordinates Network, 10060
- Perley, D. A., Hillenbrand, L., & Prochaska, J. X. 2015, GRB Coordinates Network, 18487
- Perley, D. A., Prochaska, J. X., & Morgan, A. N. 2012, GRB Coordinates Network, 14059
- Perley, D. A., Cenko, S. B., Corsi, A., et al. 2014, *ApJ*, 781, 37
- Planck Collaboration, Ade, P. A. R., Aghanim, N., et al. 2016, *A&A*, 594, A13
- Pozanenko, A., Mazaeva, E., Minaev, P., et al. 2016, GRB Coordinates Network, 19561
- Pugliese, V., Xu, D., Tanvir, N. R., et al. 2015, GRB Coordinates Network, 17672
- Racusin, J. L., Oates, S. R., de Pasquale, M., & Kocevski, D. 2016, *ApJ*, 826, 45
- Rau, A., Savaglio, S., Krühler, T., et al. 2010, *ApJ*, 720, 862
- Rees, M. J., & Meszaros, P. 1992, *MNRAS*, 258, 41P
- Rossi, A., Kruehler, T., Greiner, J., et al. 2008, GRB Coordinates Network, 8266
- Sanchez-Ramirez, R., Gorosabel, J., Castro-Tirado, A. J., Cepa, J., & Gomez-Velarde, G. 2013, GRB Coordinates Network, 14685
- Sari, R., Piran, T., & Narayan, R. 1998, *ApJL*, 497, L17
- Schlaflly, E. F., & Finkbeiner, D. P. 2011, *ApJ*, 737, 103
- Schmidl, S., Graham, J. F., & Greiner, J. 2014, GRB Coordinates Network, 16899

- Schulze, S., Wiersema, K., Xu, D., & Fynbo, J. P. U. 2014, GRB Coordinates Network, 15831
- Schulze, S., Klose, S., Björnsson, G., et al. 2011, *A&A*, 526, A23
- Singer, L. P., Kasliwal, M. M., Cenko, S. B., et al. 2015, *ApJ*, 806, 52
- Sparre, M., Sollerman, J., Fynbo, J. P. U., et al. 2011, *ApJL*, 735, L24
- Starling, R. L. C., van der Horst, A. J., Rol, E., et al. 2008, *ApJ*, 672, 433
- Tanvir, N. R., & Ball, J. 2012, GRB Coordinates Network, 13532
- Tanvir, N. R., Levan, A. J., Wiersema, K., et al. 2014, GRB Coordinates Network, 16150
- Tanvir, N. R., Wiersema, K., & Levan, A. J. 2010, GRB Coordinates Network, 11230
- Tanvir, N. R., Wiersema, K., Levan, A. J., Cenko, S. B., & Geballe, T. 2011, GRB Coordinates Network, 12225
- Tanvir, N. R., Wiersema, K., Levan, A. J., et al. 2012, GRB Coordinates Network, 13441
- Tanvir, N. R., Fox, D. B., Levan, A. J., et al. 2009, *Nature*, 461, 1254
- Tanvir, N. R., Levan, A. J., Cenko, S. B., et al. 2016, GRB Coordinates Network, 19419
- Thoene, C. C., de Ugarte Postigo, A., Gorosabel, J., et al. 2012, GRB Coordinates Network, 13628
- Troja, E., Sakamoto, T., Guidorzi, C., et al. 2012, *ApJ*, 761, 50
- Troja, E., Butler, N., Watson, A. M., et al. 2013a, GRB Coordinates Network, 14684
- . 2013b, GRB Coordinates Network, 15475
- Trotter, A., Haislip, J., Reichart, D., et al. 2014, GRB Coordinates Network, 15859
- Uehara, T., Toma, K., Kawabata, K. S., et al. 2012, *ApJL*, 752, L6
- Updike, A., Klose, S., Clemens, C., & Greiner, J. 2009a, GRB Coordinates Network, 9054
- Updike, A., Rossi, A., & Greiner, J. 2009b, GRB Coordinates Network, 10271
- Urata, Y., Huang, K., Yamaoka, K., Tsai, P. P., & Tashiro, M. S. 2012, *ApJL*, 748, L4
- Usov, V. V. 1994, *MNRAS*, 267, 1035
- van Marle, A. J., Langer, N., Achterberg, A., & García-Segura, G. 2006, *A&A*, 460, 105
- van Paradijs, J., Groot, P. J., Galama, T., et al. 1997, *Nature*, 386, 686
- Veres, P., Corsi, A., Frail, D. A., Cenko, S. B., & Perley, D. A. 2015, *ApJ*, 810, 31
- Volnova, A., Klunko, E., Eselevich, M., Korobtsev, I., & Pozanenko, A. 2014, GRB Coordinates Network, 16814
- von Kienlin, A. 2013, GRB Coordinates Network, 14473
- von Kienlin, A., Meegan, C. A., Paciesas, W. S., et al. 2014, *ApJS*, 211, 13
- Wang, X.-G., Zhang, B., Liang, E.-W., et al. 2015, *ApJS*, 219, 9
- Watson, A. M., Troja, E., Butler, N., et al. 2016, GRB Coordinates Network, 19602
- Wiersema, K., Tanvir, N., Levan, A., & Benn, C. 2009a, GRB Coordinates Network, 9995
- Wiersema, K., Tanvir, N. R., Cucchiara, A., Levan, A. J., & Fox, D. 2009b, GRB Coordinates Network, 10263
- Wijers, R. A. M. J., & Galama, T. J. 1999, *ApJ*, 523, 177
- Wijers, R. A. M. J., Rees, M. J., & Meszaros, P. 1997, *MNRAS*, 288, L51
- Woosley, S. E. 1993, *ApJ*, 405, 273
- Xu, D., de Ugarte Postigo, A., Geier, S., et al. 2015, GRB Coordinates Network, 17582
- Xu, D., Heintz, K. E., Malesani, D., & Fynbo, J. P. U. 2017, GRB Coordinates Network, 20458
- Xu, D., Heintz, K. E., Malesani, D., Wiersema, K., & Fynbo, J. P. U. 2016a, GRB Coordinates Network, 19773
- Xu, D., Levan, A. J., Fynbo, J. P. U., et al. 2014a, GRB Coordinates Network, 16983
- Xu, D., Malesani, D., Fynbo, J. P. U., et al. 2016b, GRB Coordinates Network, 19600
- Xu, D., Malesani, D., Tanvir, N. R., et al. 2014b, GRB Coordinates Network, 15645
- Xu, D., Fynbo, J. P. U., Tanvir, N. R., et al. 2009, GRB Coordinates Network, 10053
- Yates, R., Knust, F., Kann, D. A., & Greiner, J. 2015, GRB Coordinates Network, 17821
- Zhang, B., & Yan, H. 2011, *ApJ*, 726, 90